Photocatalytic defluorination of ciprofloxacin by nitrogen-defected g-C_3N_4 under simulated sunlight: mechanistic insight and pathway analysis

Yong Liu [a], Mohammadreza Kamali [a], Xiaochuan Chen [b], Barbara Rossi [c,a], Lise Appels [a], Raf Dewil [a,c,*]

[a] KU Leuven, Department of Chemical Engineering, Process and Environmental Technology Lab, J. De Nayerlaan 5, 2860 Sint-Katelijne-Waver, Belgium

[b] Fujian Normal University, College of Environmental and Resource Sciences and College of Carbon Neutral Modern Industry, Fuzhou 350000, Fujian, China.

[c] University of Oxford, Department of Engineering Science, Parks Road, Oxford OX1 3PJ, United Kingdom

* corresponding author.

Abstract: The photocatalytic degradation of ciprofloxacin (CIP) has been widely reported to be induced by ring cleavage and defluorination. However, the role of photo-generated reactive radicals, especially electrons, in defluorination remains controversial. This study investigates the effects of reactive radicals such as hydroxyl radicals (·OH) and electrons on CIP degradation and defluorination in photocatalytic processes by nitrogen-defected g-C_3N_4. Almost complete CIP degradation and 46.5% defluorination were obtained under the best conditions tested. Scavenging tests, degradation intermediate product identification, and theoretical calculations were performed to explore the reaction routes driven by ·OH and electrons in depth. Scavenging tests revealed that ·OH and electrons were predominantly responsible for direct CIP defluorination, whereas electrons played an indirect role as critical intermediates for the formation of ·OH. Time-dependent intermediate evolution analysis demonstrated that CIP degradation mainly occurred by piperazine ring cleavage and defluorination. Density functional theory (DFT) calculations based on the Hirschfeld charge, Fukui index and electrostatic potential confirmed that zwitterionic CIP^{+-} is more reactive than CIP^{+} and that the piperazine ring in CIP is susceptible to nucleophilic and radical attacks by $\cdot O_2^-$ and ·OH. Finally, electron-assisted ·OH substitution and C-F bond cleavage were proposed as the main mechanisms for CIP defluorination. This study provides a thorough understanding of CIP defluorination mechanisms by nitrogen-defected g-C_3N_4-based photocatalysis.

Keywords: photocatalysis, hydroxyl radical, electron, defluorination

1 Introduction

Ciprofloxacin (CIP) is a widely used fluoroquinolone antibiotic whose maximum detected concentrations are 3 ng/L-240 μg/L, 7 ng/L-15670 ng/L and 14 μg/L in pharmaceutical wastewater effluent, municipal wastewater, surface water and groundwater, respectively [1]. The occurrence of CIP in aquatic environments leads to toxic effects on aquatic organisms and the development of antibiotic resistance [2]. Thus, eliminating CIP from aquatic environments is of foremost importance in wastewater treatment. Advanced oxidation processes (AOPs), especially photocatalysis, have demonstrated promising potential for eliminating CIP from aquatic environments [3]. Metal-free graphitic carbon nitride (g-C_3N_4) has attracted considerable interest in the field of pollutant degradation because of its visible light sensitivity, easy synthesis, low cost and high stability. Nevertheless, the photocatalytic activity of pristine g-C_3N_4 faces the problem of fast recombination of photo-generated electron-hole pairs [4–6]. Various methodologies, such as defect engineering, doping and heterostructure construction, have been developed to enhance the separation efficiency of electrons and holes in g-C_3N_4 [5,6]. Compared to other modification techniques, defect engineering is regarded as a more facile, effective and less expensive strategy for improving the photocatalytic performance of g-C_3N_4 for pollutant decomposition [6,7]. Several studies have shown that incorporating defects, such as nitrogen and carbon vacancies, into g-C_3N_4 could tune its energy band and electronic structures to extend its light absorption range and promote the separation of electrons and holes, leading to increased photocatalytic performance [4,6,8].

In the process of CIP photocatalytic degradation, holes (h^+), hydroxyl radicals (·OH), superoxide anion radicals ($\cdot O_2^-$), singlet oxygen ($^1O_2$) and electrons are generally recognized as the dominant reactive species [9,10]. According to the existing reports, the possible photocatalytic reactions occurring during CIP degradation can generally be summarized as Eqs. (1) to (6) [2,11]. Based on the determination of degradation intermediate products (DPs), the photocatalytic degradation of CIP was suggested to most likely occur by attack of the piperazine ring and quinolone structure (including the ring structure, carboxyl group, and F), and potential degradation pathways were suggested [12]. In addition, theoretical calculations, especially DFT calculations, have been used to predict the potential reactive sites for radical, electrophilic and nucleophilic attacks in CIP according to calculated values such as frontier electron densities (FEDs), point charges and the Fukui index [13,14]. In the studies by Alhokbany *et al.* [15] and Yu *et al.* [2], FEDs and point charges on different atom sites in CIP were calculated to predict the CIP photocatalytic degradation pathway. The carbon atoms and nitrogen atoms with higher FED^2_{HOMO} (HOMO means highest occupied molecular orbital) and larger negative charge values in the piperazine ring are more easily attacked by h^+, while the carbon atoms with higher $FED^2_{HOMO} + FED^2_{LUMO}$ (LUMO means lowest unoccupied molecular orbital) in the quinoline ring are mainly attacked by ·OH. Chi *et al.* applied the Fukui function to analyze the possible reaction sites on CIP by calculating attack values defined from isosurface electron density [16]. CIP degradation mechanisms can be categorized into (i) nucleophilic attack, in which the nitrogen and carbon sites in the quinolone ring with the highest nucleophilic attack values are most prone to nucleophilic attack, and (ii) electrophilic attack, in which the piperazine rings are most likely to be cleaved through electrophilic attack at the nitrogen and carbon sites with the most positive electrophilic attack values.

$$\text{Photocatalysts} + h\nu \text{ (visible light)} \rightarrow \text{Photocatalysts} (h^+ + e^-) \quad (1)$$

$$e^- + O_2 \rightarrow \cdot O_2^- \quad (2)$$

$$\cdot O_2^- + e^- + 2H^+ \rightarrow H_2O_2 \quad (3)$$

$$H_2O_2 + e^- + H^+ \rightarrow H_2O + \cdot OH \quad (4)$$

$h^+ + H_2O \rightarrow H^+ + \cdot OH$ (5)

CIP + reactive species ($\cdot OH$, h^+, $\cdot O_2^-$ and e^-) → CO_2 + H_2O + F^- + intermediates (6)

Considerable efforts have been dedicated to investigating and revealing the photocatalytic degradation process of CIP, deciphering the degradation products and proposing degradation pathways. However, questions related to CIP defluorination remain unclear and controversial. Many intermediate products generated during the degradation process, especially those containing halogens, have been proposed to exhibit greater toxicity and carcinogenicity than the parent compounds [2]. Generally, dehalogenation reduces the toxicity of intermediate products formed from parent fluorinated organic compounds [17]. Halogenated organics are less prone to oxidation, while advanced reduction processes are suitable for their treatment owing to the efficient carbon-halogen bond breakage by reactive reducing species (i.e., hydrated electrons $\cdot e_{aq}^-$) [18,19]. On the basis of intermediate product analysis, it has been suggested by many studies that the defluorination of CIP is mainly induced by ·OH substitution in AOPs [20–22]. Nevertheless, it has also been reported that ·OH is prone to react with a strong electron-donating group, while the C-F in the benzene ring of CIP is a strong electron-withdrawing group, indicating that the substitution of F by ·OH may be difficult [23,24]. To date, neither experiments nor theoretical calculations have clarified the substitution of F in CIP by ·OH in the photocatalytic process. Notably, many studies have proposed defluorination pathways even without measuring or determining the F^- concentration after CIP degradation [25–27]. As one of the main reactive species during photocatalytic degradation, although the stable existence of electrons can be easily affected by oxidants, its potential role in CIP defluorination cannot be ignored. To the best of our knowledge, very little attention has been given to elucidating the potential role of electrons in the defluorination of CIP.

The present study was designed to investigate the underlying mechanisms of the photocatalytic degradation and defluorination of CIP by nitrogen-defected g-C_3N_4 under simulated solar light irradiation. The reactive species for CIP degradation and defluorination were determined by scavenging tests; specifically, the direct and indirect effects of ·OH and electrons on defluorination were investigated by a combination of O_2/N_2 purging and scavenging experiments. Degradation intermediate identification and DFT calculations were combined to propose the active sites for electrophilic, nucleophilic and radical attacks. Therefore, degradation and defluorination pathways were proposed based on experimental and theoretical investigations. Finally, the changes in the toxicity of the parent CIP and its degradation intermediates were evaluated using the toxicity estimation software TOOL.

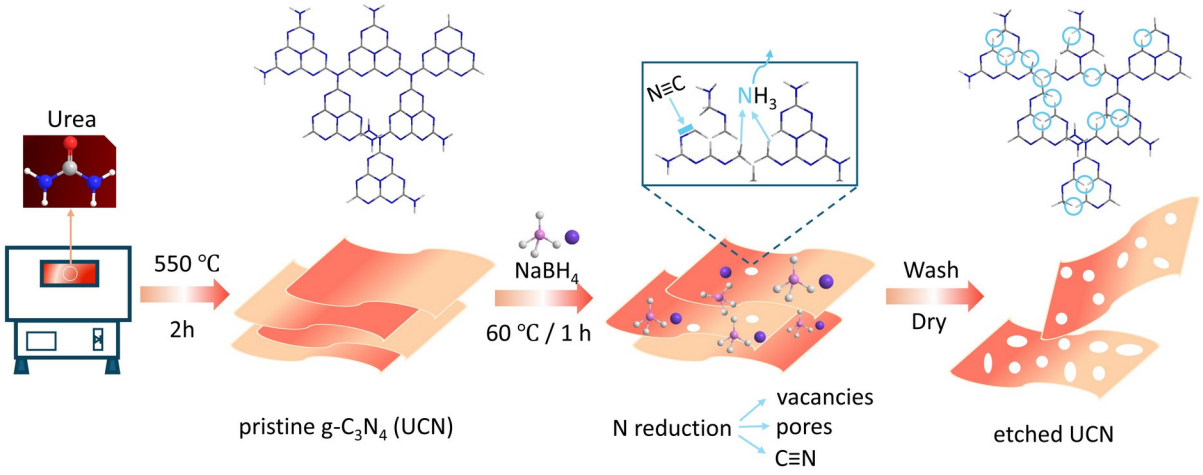
2 Experimental

Details on the chemicals, characterization and analytical methods used are provided in Text S1, Text S2, and Text S3 of the supporting information.

2.1 Sample synthesis

Urea was applied as a precursor for the synthesis of g-C_3N_4. The synthesis process of all the samples is illustrated in Scheme 1. In the first step, pristine g-C_3N_4 (denoted as UCN) was prepared by direct calcination of urea in a muffle furnace at 550 °C for 2 h at a ramp rate of 10 °C/min. The obtained UCN was further modified by sodium borohydride ($NaBH_4$) etching. Briefly, 0.4 g of UCN and 0.3 g of $NaBH_4$ were mixed and ground uniformly. Then, the mixture was dissolved in 15 mL of Milli-Q water and heated to approximately 60 ℃ for 1 h with magnetic stirring at 250 rpm. The obtained

slurry mixture sample was centrifuged to remove most of the water. Finally, the obtained etched UCN sample was washed with water and ethanol 5 times to remove impurities and dried for further use.



Scheme 1 The synthesis and modification of g-C_3N_4

2.2 Photodegradation experiments

A G2V pico LED Solar Simulator (G2V Optics Inc., Canada) with an irradiance equal to the solar equivalent (75.9 mW cm^{-2} base spectrum) was applied as the simulated solar light. The emission spectrum of the light source is shown in Fig. S1. Typically, batch photocatalytic experiments were conducted in 250 mL beakers with black jackets. Unless specifically stated, standard photocatalytic degradation experiments were carried out by illuminating 100 mL of aqueous suspension containing 5 mg/L CIP (with $[F]_0$ = 0.287 mg/L) and 0.5 g/L UCN. The temperature was 25 ± 1 ℃, and the suspension was magnetically stirred at 500 rpm to maintain good mixing. The initial pH of the 5 mg/L CIP solution was approximately 6.0, and the solution was not buffered for the experiments and was only initially adjusted with NaOH (0.1 M) and HCl (0.1 M). Specifically, pH values of 3, 4.5, 6, 7.5, 9 and 10.5 were selected to investigate the impact of pH. In the photocatalytic process with H_2O_2 (5, 10, 20, 40 mM), 1 mL of H_2O_2 storage solution (0.505, 1.01, 2.02 and 4.04 M) was added to the system immediately after the catalyst was dispersed uniformly in the suspension. In some experiments, no light illumination was applied to explore the adsorption of CIP on UCN or etched UCN and the activating effect of UCN or etched UCN on H_2O_2. Scavenging tests were conducted to explore the dominant reactive species by introducing *tert*-butanol, ammonium oxalate, silver nitrate, 1,4-benzoquinone and sodium azide to quench ·OH, h^+, e^-, $\cdot O^{2-}$ and $^1O_2$, respectively. N_2 and O_2 (0.1 L/min) were added to the bulk solution to investigate the effect of electrons on CIP degradation and defluorination. At given time intervals, aliquots of the suspension were sampled and filtered through a 0.45 μm membrane filter, and 0.25 mL of methanol was added to each 0.5 mL sample to prevent further CIP degradation by residual reactive species.

2.3 Photoelectrochemical measurements

Photoelectrochemical experiments were carried out in a three-electrode system by using an Autolab 200 N electrochemical workstation (Autolab, Metrohm). A catalyst coated with indium-tin oxide (ITO) glass (resistance 8-12 Ω, Sigma–Aldrich), an Ag/AgCl (saturated KCl) electrode, a Pt wire and 0.5 M Na_2SO_4 (pH 6.8) were utilized as the working electrode, reference electrode, counter electrode and electrolyte, respectively. For the preparation of the working electrode, ITO was first washed in ethanol and Milli-Q water by ultrasonication, and then the catalyst ink was prepared by dispersing 5 mg of catalyst in a 1 mL solution containing 20 μL of 5 wt.% Nafion, 500 μL of isopropanol and 480 μL of Milli-Q water with subsequent ultrasonic bath treatment for 30 min. Afterwards, the obtained ink was drop-cast onto the pretreated ITO. Electrochemical impedance spectroscopy (EIS) was

performed to detect the electrolyte resistance over a frequency range from 0.1 Hz to 100 kHz. Mott–Schottky plots were collected between -0.4 and +0.4 V at a frequency of 5000 Hz.

All obtained potentials were converted to the normal hydrogen electrode (NHE) potential (E_{NHE}) as follows [28]:

$$E_{NHE} = E_{Ag/AgCl} + E^{0}_{Ag/AgCl}$$

Where $E^{0}_{Ag/AgCl}$ = 0.1976 V at 25 ℃, $E_{Ag/AgCl}$ is experimentally determined against the Ag/AgCl reference electrode.

2.4 Theoretical calculation methods

Gaussian 16 A.03 software was used for all reaction calculations in this study. M06-2X with the 6–311g (d.p.) basis set was used to optimize the geometry. The solute electron density (SMD) was selected as the solvent for the simulation of CIP oxidation in water [29]. Theoretical calculations of the natural population analysis (NPA) charge and condensed Fukui function were realized by Multiwfn 3.8 (dev) [30], and then visual molecular dynamics (VMD 1.9.3) was used to display the color-mapped electrostatic potential isosurface images [31].

3 Results and discussion

3.1 Characterization

The surface morphology of a photocatalyst can influence its catalytic performance by altering the availability of active sites and the presence of surface functional groups. It can be seen from the SEM images in Fig. 1(a) and Fig. 1(d) that the pristine UCN shows a thick curled nanosheet with bulky aggregation, while the etched UCN displays a thinner nanosheet stacked structure with fewer blocks and more pores. In Fig. 1(b-c) and Fig. 1(e-f), TEM was further employed to observe the detailed surface differences of the as-prepared UCN samples. An ultrathin silk-like structure can be clearly identified in both pristine and etched UCN. In addition, the TEM images further confirmed that more blocks stacked together, and few pores were observed on the surface of the pristine UCN, whereas fewer blocks and numerous newly generated pores (Fig. 1(f)) were distinctly observed on the surface of the etched UCN due to $NaBH_4$ etching. The SEM and TEM results provide evidence that $NaBH_4$ etching improved the porous structure of UCN. The improved porous structure of etched UCN is beneficial for providing more active sites for not only adsorption but also photocatalytic reactions when it is used as a photocatalyst for contaminant degradation [32]. As shown in Fig. 1(g-i) and Fig. S2, EDS and mapping were performed to investigate the elemental composition and distribution on the etched UCN. According to these images, C and N were distributed uniformly on both pristine UCN and etched UCN. Notably, EDS mapping of etched UCN revealed irregular holes (i.e., the area in the red circle) without the presence of C and N, as shown in Fig. 1(g-i), confirming the successful incorporation of pores and implying the potential generation of nitrogen vacancies in etched UCN by $NaBH_4$ treatment. In addition, the total nitrogen (TN) and total carbon (TC) determination results in Table S1 indicate that the C/N ratio in etched UCN is 1.69 times that of pristine UCN, confirming the removal of nitrogen by $NaBH_4$ treatment.

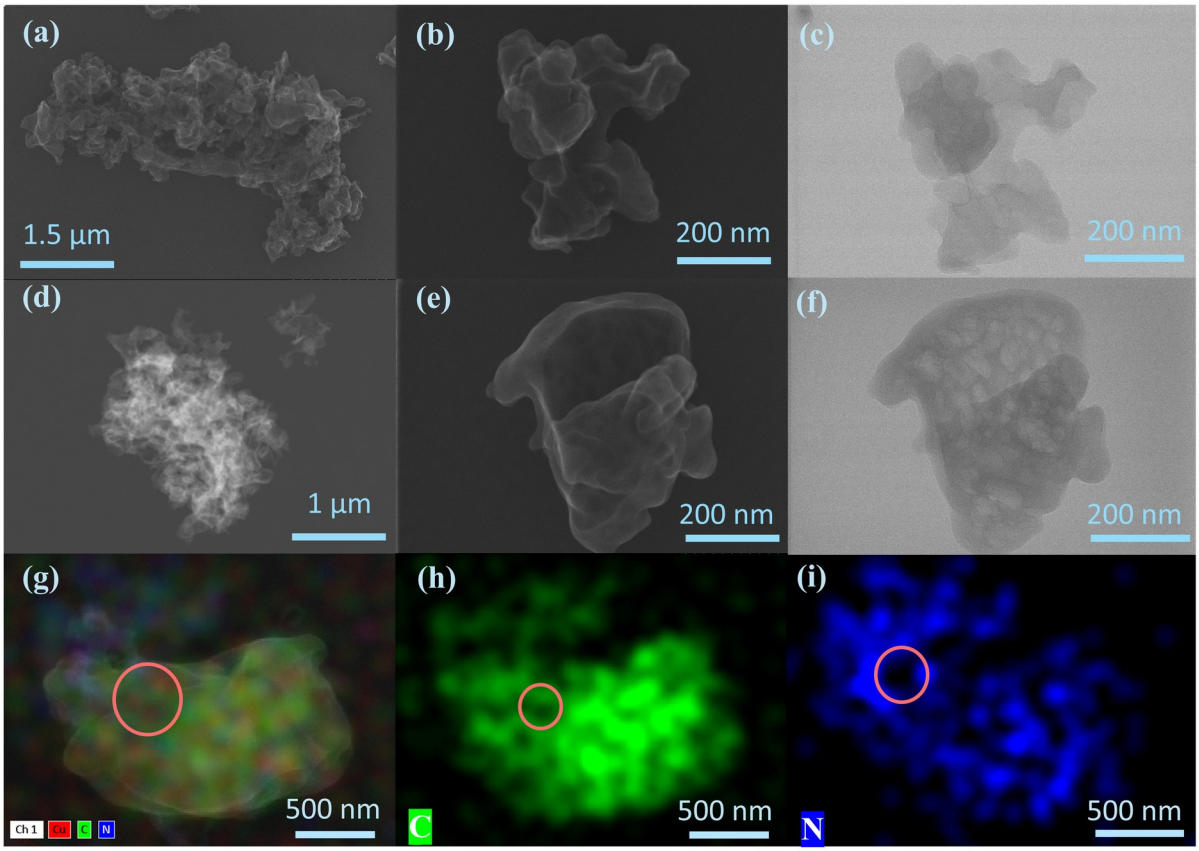


Fig. 1. SEM images of pristine (a) and etched (d) UCN, STEM images of pristine (b-c) and etched (e-f) UCN, and corresponding elemental mapping images of etched UCN (g-i).

XRD was carried out to investigate the crystal structure of the prepared UCN samples. In Fig. 2(a), two diffraction peaks located at 22.1° and 12.2° are observed in both pristine UCN and etched UCN, which are assigned to the sheet interlayer stacking (002) and the in-plane structural packing of triazine units (100) of g-C_3N_4, respectively [33]. The intensity of the (100) diffraction peak weakens in the spectrum of etched UCN, implying that $NaBH_4$ treatment may lead to the collapse of a uniform planar structure by generating nitrogen vacancies.

FTIR was applied to examine the surface functional group changes in UCN induced by the $NaBH_4$ treatment. It can be seen from Fig. 2(b-c) that the FTIR spectrum of etched UCN is similar to that of pristine UCN, suggesting that the basic structure is preserved after $NaBH_4$ treatment. The broad peak at 2900–3300 cm^{-1} is attributed to N-H stretching vibration, as well as -OH from the adsorbed H_2O on the surface of the catalysts. The peaks at 1700–1250 cm^{-1} are ascribed to the stretching vibrations of the C=N and C-N heterocycles, and the distinct peak at 805 cm^{-1} corresponds to the vibration of triazine units [34,35]. After $NaBH_4$ treatment, a new peak corresponding to C≡N appears at approximately 2180 cm^{-1} in the spectrum of etched UCN, indicating that the triazine unit in UCN may be cleaved by $NaBH_4$ treatment to introduce molecular structural defects [36]. In addition, the intensity and width of the characteristic peaks at 1456 and 1551 cm^{-1} in the spectrum of etched UCN are very weak compared to those of its pristine counterpart, suggesting the breaking of carbon-nitrogen bonds and the formation of nitrogen vacancies in etched UCN. Generally, there are three different N sites in g-C_3N_4 (i.e., the N1 site of the N-C bridging structure connecting heptazine units, the N2 site of the C-N-C coordination structure in a heptazine unit, and the N3 site of central N in a heptazine unit), as depicted in Fig. S3, among which N1 and N2 are easier to reduce into NH_3, while central N3 is hard to reduce owing to its greater stability [33].

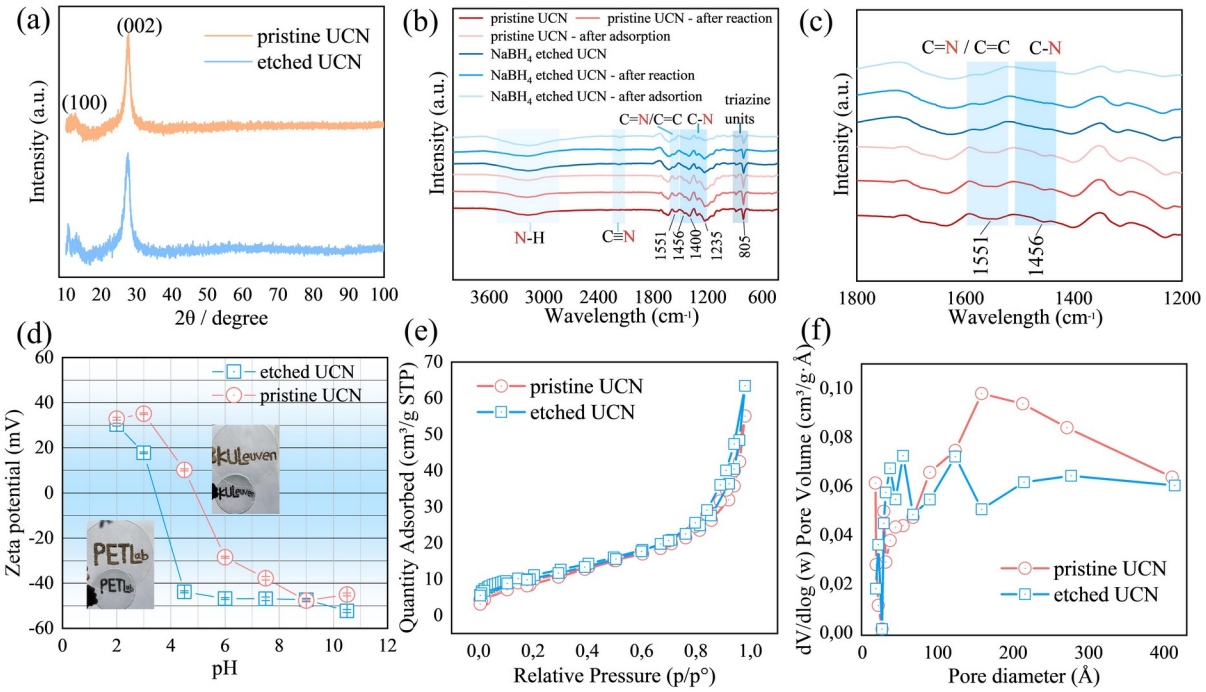


Fig. 2. XRD patterns (a), FTIR spectra (b-c), zeta potentials (d) and BET surfaces (e-f) of pristine UCN and etched UCN.

The zeta potential was studied as an indicator of the surface charge of the UCN samples, as shown in Fig. 2(d). The zeta potential of the etched UCN was more negative than that of the pristine UCN over the entire measured pH range. Specifically, the isoelectric points of etched UCN and pristine UCN are 3.42 and 4.87, respectively. The enhanced isoelectric point of etched UCN might be due to the generation of C≡N [36]. As shown in Fig. 2(e), the $NaBH_4$ treatment increased the BET surface area of UCN from 35.60 to 39.81 m^2/g. The Barrett–Joyner–Halenda (BJH) model was applied to examine the pore size distribution of the UCN samples, as shown in Fig. 2(f). The pore size distribution of pristine UCN is mainly centered at 30.1 and 160.3 Å, while that of etched UCN is wider, with peak centers located at approximately 21.7, 35.9, 53.4 and 125.3 Å, implying that etched UCN contains nearly micropores and abundant mesopores. The difference in pore size distribution between UCN samples further confirms the improved porous structure in etched UCN, where the micro- and mesopores may provide more active sites for adsorption and photocatalysis [37].

3.2 Photoelectrochemical properties

Electrochemical impedance spectroscopy (EIS) was performed to evaluate the transfer efficiency of the photogenerated charge carriers, as shown in Fig. 3(a). In general, the radius of the arc in Nyquist plots is positively correlated with the charge transfer resistance (R_t) [38,39]. Fig. 3(a) indicates that etched UCN displays a smaller radius than pristine UCN, implying that the improved porous structure and incorporated nitrogen vacancies are beneficial for improving the charge transfer efficiency. In addition, the Nyquist curves could be well fitted to the simulated electrical equivalent circuit model, as depicted in the inset figure. The obtained fitting data (Table S2) were consistent with the results of the Nyquist plots.

In Fig. 3 (b), the light absorption capacity of pristine UCN and etched UCN was determined by UV–vis diffuse reflectance spectroscopy (DRS), and the band gap was calculated, as shown in Fig. 3(c). Compared with that of its pristine counterpart, the light absorption edge of the etched UCN redshifted

to 484 nm. The bandgap energies of pristine UCN and etched UCN were calculated to be 2.12 and 2.69 eV, respectively, according to the Kubelka–Munk function, as shown in Eq. (7) [40].

$$\alpha h\nu = A(h\nu - E_g)^{n/2} \quad (7)$$

where α, h, ν, A and E_g represent the absorption coefficient, Planck constant, light frequency, constant and bandgap energy, respectively. The n value of UCN is determined to be 1 based on the optical transition properties of semiconductors [40,41].

The reduction and oxidation capability of the photogenerated electrons and holes is dependent on the potential of the conduction band (E_{CB}) and valence band (E_{VB}) of a photocatalyst [39]. Mott–Schottky plots were obtained to study the energy structure of pristine UCN and etched UCN. Fig. 3(d) shows that both pristine UCN and etched UCN displayed positive slopes, confirming that they are n-type semiconductors. The flat band potential (E_{ft}) is reported to be approximately equal to the Fermi level potential in n-type semiconductors [42,43]. The flat band potentials of pristine UCN and etched UCN were -0.62 and -0.38 eV (vs. Ag/AgCl, pH = 6.5), corresponding to -0.42 and -0.18 eV vs. NHE, respectively. It is widely accepted that the flat band potential of an n-type semiconductor is approximately 0-0.1 eV lower than that of its E_{CB} [43]. Here, 0.05 eV was set as the difference benchmark, and the E_{CB} of pristine and etched UCN was calculated to be -0.47 and -0.23 eV vs. NHE, respectively. Hence, the energy band alignments of pristine UCN and etched UCN are schematically presented in Fig. 3(e). The above results indicate that the band and electronic structures of UCN were obviously tuned after $NaBH_4$ treatment.

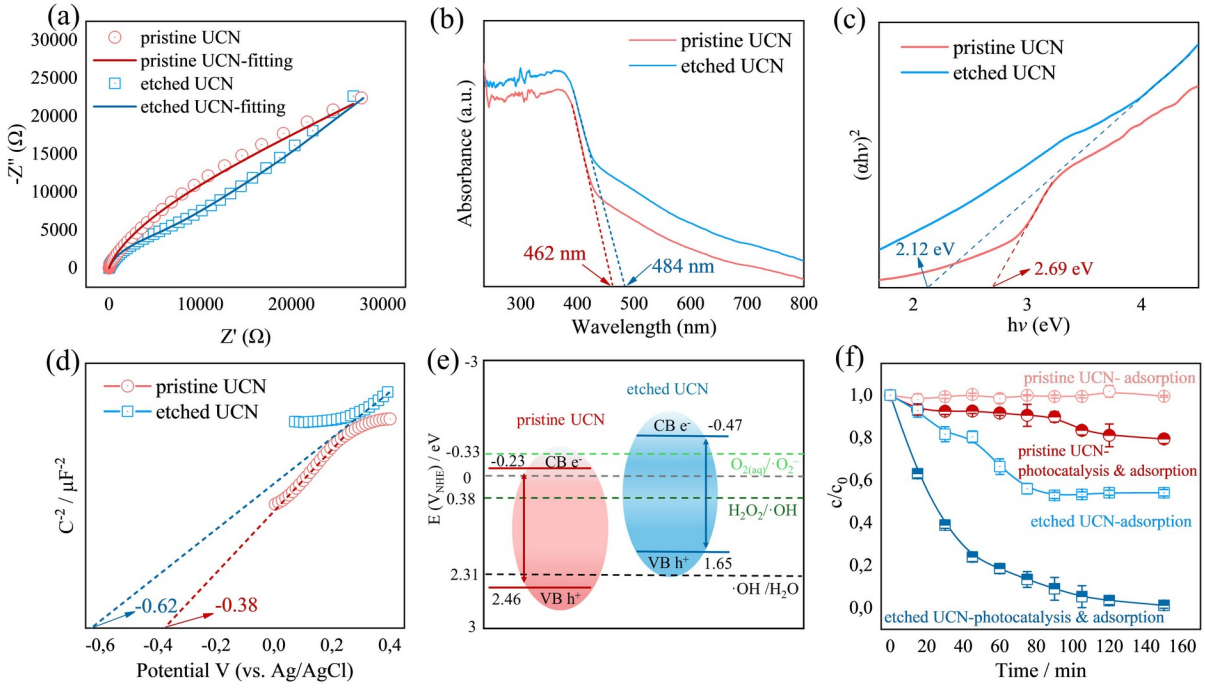


Fig. 3 Electrochemical impedance spectroscopy (a), UV–Vis diffuse reflectance spectra (b), plots of the transformed Kubelka–Munk function versus photon energy, Mott−Schottky plots (d), proposed band structures of pristine UCN and etched UCN (e), and photocatalytic degradation and adsorption of CIP by etched UCN and pristine UCN (f); conditions: $[CIP]_0$ = 5 mg/L (with $[F]_0$ = 0.287 mg/L), initial pH ≈ 6.0, [etched/pristine UCN] = 0.5 g/L, and simulated sunlight.

3.3 Enhanced photocatalytic properties of etched UCN

Adsorption and photocatalysis have synergistic effects on the degradation of antibiotics. Adsorption of antibiotics on the surface of photocatalysts is the first step for efficient photocatalytic degradation, while photocatalysis can reproduce the effective adsorption sites on photocatalysts. In Fig. 3(f), the

pristine UCN showed limited adsorption and lower photocatalytic degradation for CIP, while distinct improvements in both properties were observed for the etched UCN. The underlying mechanisms for the adsorption of antibiotics on catalysts can be categorized into hydrophobic interactions, hydrogen bonding, π-π electron donor−acceptor (EDA) interactions and electrostatic interactions by coulombic forces [44,45]. Physical adsorption is highly dependent on the surface properties of the adsorbent (i.e., specific surface area, pore size and surface charge). The zeta potentials of the etched UCN and pristine UCN were 3.42 and 4.87, respectively. As discussed above, the species of CIP and its charge are dependent on pH, as shown in Fig. S4. The initial pH of the CIP solution was 5.95-6.03, and the dominant CIP species were CIP^{+} and CIP^{+-}. Pristine UCN with a negative surface charge at pH 5.95-6.03 exhibited little adsorption ability for the dominant CIP species, suggesting that physical adsorption is not the dominant mechanism for this adsorption process. The etched UCN exhibited good adsorption of CIP at the same pH, implying that electrostatic interactions may contribute to this adsorption process. The impact of pH on the adsorption of CIP by etched UCN was further explored, as shown in Fig. S5. The results demonstrated that pH significantly influenced CIP adsorption on etched UCN, where the greatest adsorption was observed in the pH range of 4.5-6, which was attributed to electrostatic interactions owing to the opposite charges between CIP and the etched UCN. Electrostatic repulsion was expected to occur between CIP and the etched UCN at pH 3 and pH 10.5 due to the same charge, where rather limited CIP adsorption by the etched UCN was observed. In addition, hydrophobic interactions might have an important effect on CIP adsorption due to changes in CIP hydrophobicity under various pH conditions. Zwitterionic CIP^{+-} is considered to have the greatest hydrophobicity due to its low solubility at pH 7 [46,47]. In the pH range of 7.5-9, CIP mainly consists of $CIP^{+\ -}$ and CIP^{+} simultaneously. As the pH increases from 7.5 to 9, the dominant CIP species transforms from CIP^{+-} to CIP^{+}, where the electrostatic interaction might be weakened while the hydrophobic interaction improved to benefit the adsorption of CIP on etched UCN. As shown in Fig. 2(b), FTIR spectra were also recorded for UCN before and after the reaction. No obvious changes were observed on pristine UCN after either photocatalysis or adsorption of CIP, demonstrating limited CIP removal by pristine UCN, which is consistent with the experimental results. For etched UCN, the characteristic peak at 1551 cm^{-1}, corresponding to C=N and C=C, slightly strengthened after CIP adsorption, which may be ascribed to the adsorption of CIP. Comparatively, the peak intensity of the broad peak at 2900–3300 cm^{-1} in the spectrum of etched UCN increased after adsorption, which may be due to the complexation of CIP with oxygen-containing groups in etched UCN by hydrogen bonding.

A high adsorption capacity is beneficial for the subsequent photocatalytic degradation of CIP. Fig. 3(f) shows that the photocatalytic performance of etched UCN was dramatically improved. The EIS results indicate that etched UCN has a smaller charge transfer resistance than pristine UCN, leading to a better photogenerated electron-hole separation efficiency. The DRS results show that the introduction of nitrogen vacancies reduces the bandgap energy of etched UCN and enhances its light absorbing capability. Moreover, the conduction band potential of the etched UCN also shifted after $NaBH_4$ treatment. The improved photogenerated electron-hole separation efficiency and reduced bandgap energy contributed to the improved photocatalytic performance of the etched UCN. As discussed above, there are three distinct types of N sites in g-C_3N_4, which could correspond to the potential generation of diverse types of nitrogen vacancies with different effects. The synthesis of etched UCN was optimized to determine the optimal treatment time by $NaBH_4$, as shown in Fig. S6. The results suggested that after 1 h of $NaBH_4$ treatment, the etched UCN exhibited the best photocatalytic performance, implying that the number and position of the generated nitrogen vacancies may have a critical influence on the properties of the materials and their photocatalytic effect.

3.4 Photocatalytic degradation and defluorination of CIP by etched UCN

The above experimental results showed that the etched UCN exhibited good performance for CIP photocatalytic degradation. In addition, the defluorination of CIP also matters, in which ·OH has been proposed to be the dominant reactive species. Hence, H_2O_2 was added in the following experiments to investigate the defluorination mechanism. In Fig. 4(a), CIP degradation and defluorination by etched UCN were evaluated with different processes: etched UCN under simulated solar light, etched UCN in the dark, etched UCN/H_2O_2 under simulated solar light, etched UCN/H_2O_2 in the dark, and H_2O_2 under simulated solar light. Excellent CIP degradation (99.7%) and minor defluorination (1.58%) were observed with etched UCN under simulated solar light irradiation. Negligible defluorination was observed for both etched UCN in the dark and etched UCN/H_2O_2 in the dark, where the CIP removal trend was consistent with that in the case of CIP adsorption by etched UCN. The CIP removal and defluorination efficiencies were 21.2% and 3.57%, respectively, when H_2O_2 was combined with light irradiation, indicating that ·OH could be slightly generated by H_2O_2 photolysis directly under simulated solar light irradiation and may play a critical role in defluorination. Substantial increases in both defluorination and degradation efficiency were observed for etched UCN/H_2O_2 with light irradiation, where 99.9% degradation and 40.6% defluorination efficiency were obtained, respectively. From the UHPLC spectra of CIP removal at different sampling intervals by etched UCN/ H_2O_2 with and without simulated solar irradiation in Fig. S7, few degradation intermediates were detected in the process without light irradiation, while several intermediate peaks were detected in the process with light illumination, implying that H_2O_2 could be activated by etched UCN under simulated solar light to produce ·OH for CIP degradation and defluorination. The degradation and defluorination of CIP by etched UCN and etched UCN/H_2O_2 were well fitted by pseudo-first-order kinetics ($R^2 \geq 0.937$). The highest degradation (0.058 min^{-1}) and defluorination (0.007 min^{-1}) rates were obtained in the process of etched UCN/H_2O_2 under simulated solar light irradiation.

The distinctly enhanced defluorination achieved by adding H_2O_2 to the process with etched UCN under simulated solar light suggested that there was a synergistic effect between the etched UCN and H_2O_2. According to Eq. (4), the photo-generated electrons can activate H_2O_2 to generate ·OH. As shown in Eq. (5), the photogenerated h^+ with a band potential more positive than E^0 (·OH / H_2O) = 2.31 V_{NHE} at pH 7 was able to oxidize water to produce ·OH [48,49]. Fig. 3(e) shows that the valance band potential of etched UCN (1.65 eV vs. V_{NHE}) is not positive enough to oxidize water to produce ·OH. To further elucidate the role of ·OH in CIP defluorination, the effect of the added H_2O_2 concentration was investigated. As depicted in Fig. 4(c), a similar decreasing trend in the CIP concentration was observed for etched UCN/H_2O_2 with different H_2O_2 additions in the dark, which could be attributed to the adsorption effect of etched UCN, further suggesting that negligible H_2O_2 could be activated by etched UCN without simulated solar light irradiation. Comparatively, under simulated solar light irradiation, the defluorination efficiency had a positive correlation with the added H_2O_2 concentration, where the highest defluorination efficiency (46.52%) was obtained at 40 mM H_2O_2. Fig. 4(d) shows that the reaction rates of CIP degradation and defluorination initially increased from 0.034 to 0.058 min^{-1} and from 0.001 to 0.007 min^{-1}, respectively, as the H_2O_2 concentration increased from 0 to 20 mM but further decreased to 0.036 and 0.006 min^{-1}, respectively, from 20 to 40 mM. The decreased reaction rates and highest defluorination efficiency obtained with 40 mM H_2O_2 imply that ·OH may be unnecessarily consumed by H_2O_2 at high H_2O_2 concentrations, as shown in Eq. (8)-(9) [50,51], and confirm that ·OH contributes to CIP defluorination, which will be further discussed in section 3.4.1-3.4.3.

$$H_2O_2 + \cdot OH \rightarrow HO_2\cdot + H_2O \quad (8)$$

$$HO_2\cdot + \cdot OH \rightarrow H_2O + O_2 \quad (9)$$

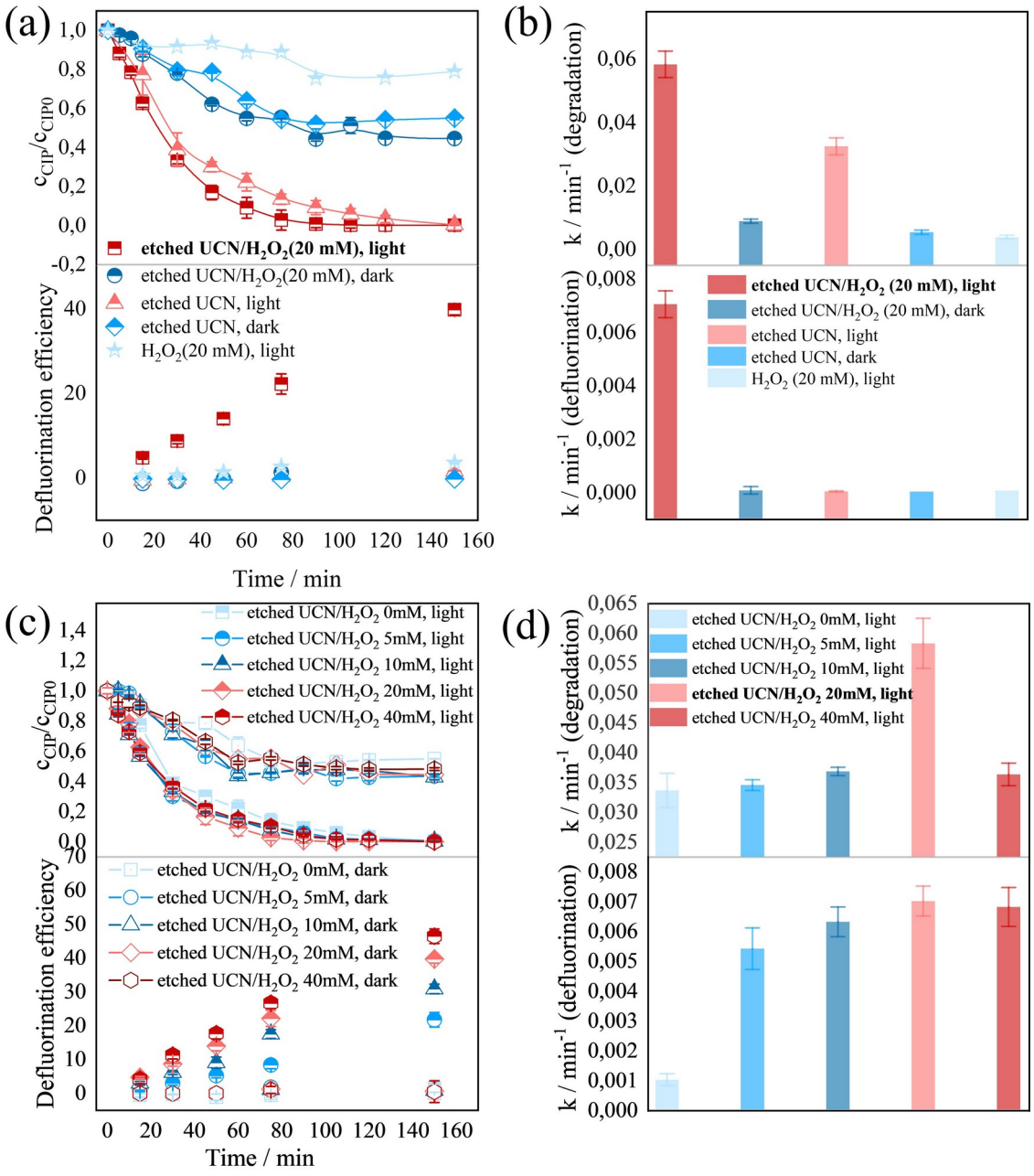


Fig. 4 CIP degradation and defluorination efficiencies (a) and corresponding reaction rates (b) under different conditions: $[CIP]_0$ = 5 mg/L (with $[F]_0$ = 0.287 mg/L), initial pH ≈ 6.0, [etched UCN] = 0.5 g/L, $[H_2O_2]$ = 20 mM, and simulated sunlight; the effect of H_2O_2 concentration (c-d), conditions: $[H_2O_2]$ = 0, 5, 10, 20 and 40 mM.

3.4.1 Effect of pH

As discussed above, the pH could influence the adsorption of CIP on etched UCN by altering the hydrophobic interactions and electrostatic interactions of the UCN. The impact of pH on CIP degradation and defluorination by etched UCN was further investigated, as shown in Fig. 5(a-b). In the pH range of 3-10.5, the degradation of CIP in the processes of etched UCN/H_2O_2 and etched UCN under simulated solar light followed pseudo-first-order kinetics (R^2 > 0.912), among which the maximum *k* values (0.0583 min^{-1} and 0.03363 min^{-1}) were both observed at pH 6, with CIP^+ and CIP^{+-} as the main dissociations. Moreover, the defluorination of CIP in the process of etched UCN/H_2O_2 also followed pseudo-first-order kinetics (R^2 > 0.957), and the highest *k* value (0.007 min^{-1}) was

observed at pH 6. Notably, negligible defluorination was observed in the process of etched UCN at different pH values, which is consistent with the above experimental results for the processes without H_2O_2. The changes in CIP degradation at different pH values were consistent with the changes in CIP adsorption by the etched UCN shown in Fig. S5, indicating that adsorption was an important prerequisite for photodegradation. The differences in CIP degradation and defluorination at different pH values could be attributed to the following complex mechanisms: (i) electrostatic interactions, where the electrostatic repulsion between CIP and etched UCN at pH 3 and 10.5 could reduce the adsorption of CIP on etched UCN; and (ii) CIP reactivity, where different CIP dissociations displayed various reactivities. It has been reported that F in different CIP species can be substituted by ·OH [1]. In the study by Wei *et al.*, the reactivity of different CIP species was investigated by computing the Gibbs free energy changes, enthalpy changes and activation free energies of their defluorination reactions. Their results indicated that C-F cleavage in CIP^+ could occur spontaneously and more easily due to the lower activation free energy of CIP^+ [52]. This is consistent with our experimental results that the maximum defluorination efficiency was observed at pH 6, with CIP^+ as the main dissociation.

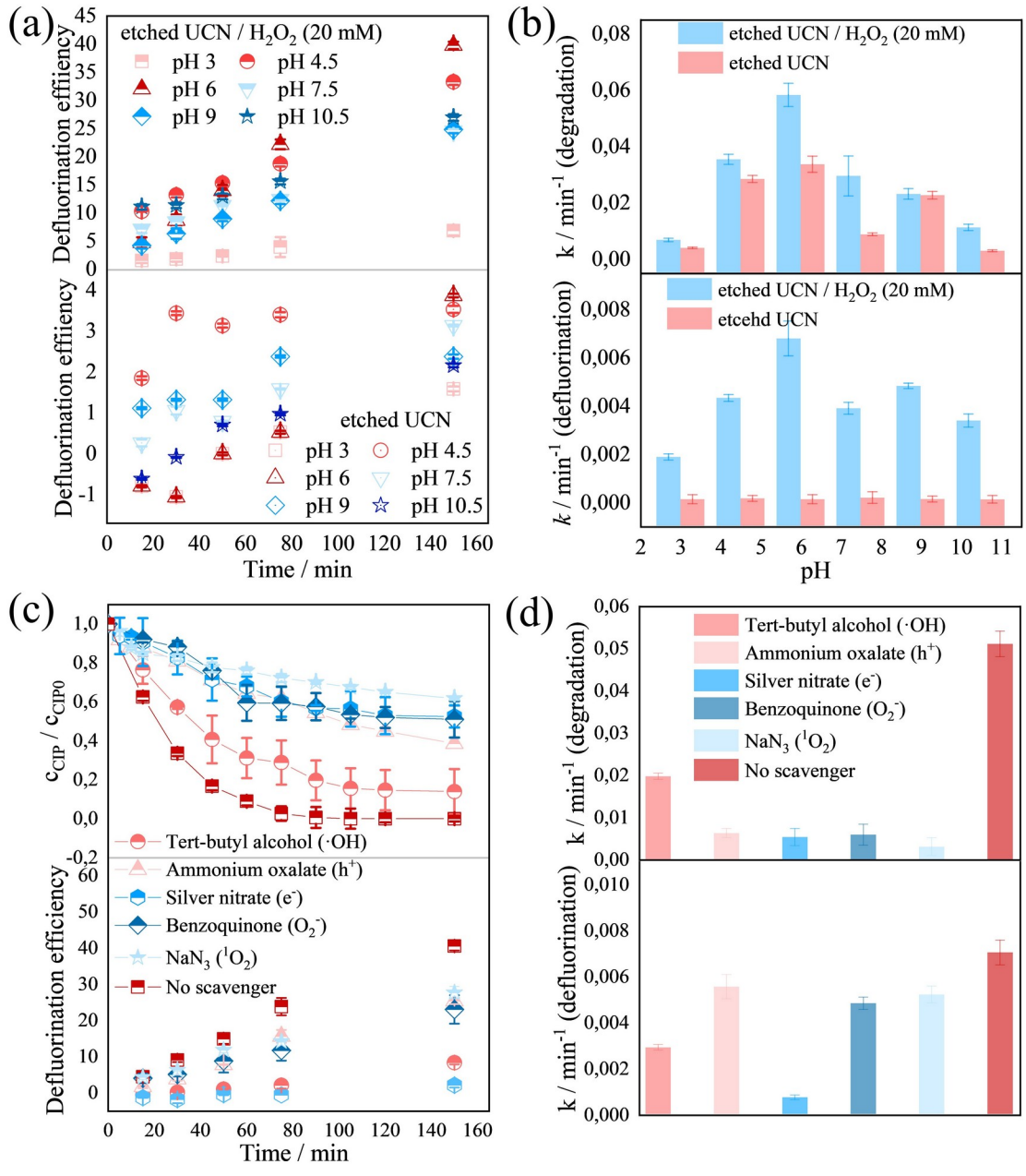


Fig. 5 The effect of pH on CIP degradation and defluorination in the processes with etched UCN/H_2O_2 and etched UCN (a-b) under the following conditions: $[CIP]_0$ = 5 mg/L (with $[F]_0$ = 0.287 mg/L), [etched UCN] = 0.5 g/L, $[H_2O_2]$ = 20 mM, pH = 3, 4.5, 6, 7.5, 9 and 10.5, and simulated sunlight; in the process with etched UCN/H_2O_2 (c-d) under the following conditions: $[CIP]_0$ = 5 mg/L (with $[F]_0$ = 0.287 mg/L), initial pH ≈ 6.0, [etched UCN] = 0.5 g/L, $[H_2O_2]$ = 20 mM, and simulated sunlight, [tert-butyl alcohol] = 10 mM, [ammonium oxalate] = 10 mM, [silver nitrate] = 10 mM, and [benzoquinone] = 5 mM.

3.4.2 The roles of reactive species

The CIP degradation and defluorination efficiencies reached 99.9% and 40.6%, respectively, in the process with etched UCN/H_2O_2 under simulated solar light. Five common photogenerated reactive radicals, including ·OH, h^+, $\cdot O^{2-}$, $^1O_2$ and electrons, were first evaluated based on their contributions to the degradation and defluorination of CIP in the presence of tert-butyl alcohol, ammonium oxalate, benzoquinone, sodium azide and silver nitrate. Fig. 5(c-d) shows that adding different quenchers could inhibit the degradation and defluorination efficiencies to a certain extent, indicating that all these reactive species were involved in the photocatalytic process. With the addition of tert-butyl alcohol, a slight decrease in degradation efficiency (86%) and a distinct decrease in defluorination efficiency (8.39%) in the system were observed, suggesting that hydroxyl radicals play a significant role in the defluorination of CIP. With the addition of ammonium oxalate, the CIP degradation efficiency obviously decreased (61.2%), and an inhibitory effect on defluorination (25.4%) was also observed. h^+ has been widely accepted to play a vital role in direct CIP degradation [[11], while the decrease in CIP defluorination implies its potential effect on defluorination in our system. In the case of the electron trapping test, dramatic inhibitory effects on both degradation (48.5%) and defluorination (2.18%) were observed with the introduction of silver nitrate. It is noted that hydrated electrons (e_{aq}^-, E_0 = -2.9 ~-2.6 V) are expected to be generated for the efficient treatment of halogenated organic compounds in advanced reduction processes [53,54], while they could hardly be produced in our system because the conduction band potential of etched UCN (-0.47 eV vs. NHE) is not negative enough for forming e_{aq}^-. Considering the intermediate role of electrons in the formation of $\cdot O_2^-$ (Eq. 2) and ·OH (Eq. 4), the significant decrease in CIP degradation and defluorination could be ascribed to the limited generation of other reactive species, especially $\cdot O_2^-$ and ·OH. The direct effect of electrons on defluorination is still unclear and will be further investigated in section 3.4.3. The CIP degradation and defluorination efficiencies were 48.9% and 23.1%, respectively, in the $\cdot O_2^-$ trapping test, further confirming the speculated role of $\cdot O_2^-$ in CIP degradation in the electron trapping test. The decreased defluorination efficiency with the introduction of benzoquinone may be induced by the inhibition of additional ·OH production from $\cdot O_2^-$, as shown in Eq. (10) [11]. In addition, it has been reported that $\cdot O_2^-$ might act as an important intermediate for the formation of $^1O_2$, as shown in Eq. (11). Hence, the potential role of $^1O_2$ was further investigated. The addition of NaN_3 significantly inhibited CIP degradation (%), indicating the dominant role of $^1O_2$ in degrading CIP. The defluorination efficiency was slightly reduced, which may also be attributed to the reduction of ·OH resulting from the consumption of $\cdot O_2^-$.

$$\cdot O_2^- + 2H^+ + 2e^- \rightarrow \cdot OH + OH^- \quad (10)$$

$$\cdot O_2^- + 2H_2O \rightarrow H_2O_2 + {}^1O_2 \quad (11)$$

A comparison of the five different trapping tests showed that (i) CIP defluorination is highly dependent on ·OH, (ii) $^1O_2$, h^+ and $\cdot O_2^-$ play critical roles in CIP degradation, and (iii) electrons play a pivotal intermediate role in the formation of ·OH and $\cdot O_2^-$. Nonetheless, the direct effect of electrons on defluorination deserves further investigation.

3.4.3 The role of photogenerated electrons

As discussed above, electrons may be involved in the defluorination of CIP via two pathways: (i) by indirectly acting as an intermediate to boost the production of ·OH for further defluorination, as described in the scavenger tests, and (ii) by direct attack. Direct defluorination by electron attack has rarely been reported due to electron instability in AOPs. The stability of photogenerated electrons in photocatalytic systems is mainly influenced by the separation efficiency of electron–hole pairs and trapping by oxidants, such as oxygen. Nitrogen vacancies have been shown to promote the separation efficiency of electron-hole pairs in etched UCN. The impact of oxygen on the electron-involving defluorination process was further investigated by atmosphere sparging tests, as shown in Fig. 6(a-b). The dissolved oxygen concentrations were approximately 0.32-0.75, greater than 22 and 7.8 mg/L in the N_2, O_2 purging and ambient environments, respectively. In principle, a lower dissolved oxygen concentration was expected to enhance the electron stability in the system. Notably, the potentials for producing ·OH and $\cdot O_2^-$ by the reaction of electrons with H_2O_2 and dissolved oxygen are 0.38 V vs. NHE ($E_0(H_2O_2/\cdot OH)$ and -0.33 V vs. NHE ($E_0(O_{2(aq)}/\cdot O_2^-)$ [55], respectively, indicating that electrons photogenerated (E_{CB}=-0.47 vs. NHE) by etched UCN could simultaneously react with H_2O_2 and dissolved oxygen. Alternatively, the generated $\cdot O_2^-$ could further react with electrons to produce ·OH (Eq. 10) [56]. Fig. 6(a-b) shows that 91.7% CIP degradation and 57.1% defluorination efficiency were achieved in the processes of etched UCN/H_2O_2 with O_2 purging. Comparatively, 99.4% CIP degradation (k = 0.0299 min^{-1}) and 8.2% defluorination efficiency were observed in the processes of etched UCN with O_2 purging. The promoted CIP defluorination efficiency in the process with etched UCN under O_2 purging compared to that of the reference without O_2 purging could be due to the additional formation of $\cdot O_2^-$, $^1O_2$ and ·OH via the reaction of electrons with O_2. Notably, $\cdot O_2^-$ might be unnecessarily consumed by H_2O_2 (Eq. 12), leading to the compromise of CIP degradation to some extent, which might explain why the reaction rate of CIP degradation in the process of etched UCN/ H_2O_2 with O_2 purging (k = 0.0157 min^{-1}) was lower than that of the process of etched UCN with O_2 purging (k = 0.0299 min^{-1}).

$$H_2O_2 + \cdot O_2^- \rightarrow \cdot OH + O_2 + OH^- \quad (12)$$

In the case of etched UCN/H_2O_2 with N_2 purging, the CIP degradation and defluorination efficiencies reached approximately 98.8% and 43.3%, respectively. CIP degradation efficiency of 97.5% and defluorination efficiency of 4.0% were obtained by etching UCN with N_2 purging. Since limited oxygen was dissolved in the processes with N_2 purging, limited amounts of extra $\cdot O_2^-$ and ·OH could be produced via electrons reacting with O_2. Similar reaction rates of CIP degradation in the processes of etched UCN/H_2O_2 and etched UCN with N_2 purging further elucidate the limited amount of $\cdot O_2^-$ in these processes. In contrast, the defluorination efficiency increased slightly from 40.6% to 43.3% in the process of etched UCN with N_2 purging compared to that of the reference without N_2 purging, which may be due to the limited consumption of H_2O_2 by $\cdot O_2^-$. Notably, the electrons can still be captured by the remaining low concentration of dissolved oxygen (0.75-1.32 mg/L) in the process of etched UCN with N_2 purging to generate $\cdot O_2^-$ and ·OH for CIP degradation and defluorination. In other words, the underlying mechanism of slight defluorination (4.0%) in the process of etched UCN with N_2 purging may be attributed to attack by ·OH or electrons. Therefore, tert-butyl alcohol and silver nitrate were further introduced into the process of etched UCN with N_2 purging as ·OH and electron scavengers to investigate the potential direct/indirect effect of electrons on defluorination. Little F^- was detected after the addition of tert-butyl alcohol, further confirming the critical role of ·OH in defluorination. With the addition of silver nitrate, little defluorination occurred due to the insufficient generation of ·OH, further confirming that (i) electrons play a critical intermediate role in the production of ·OH and (ii) the generated ·OH dominantly contributed to the defluorination of CIP and its F-containing intermediates.

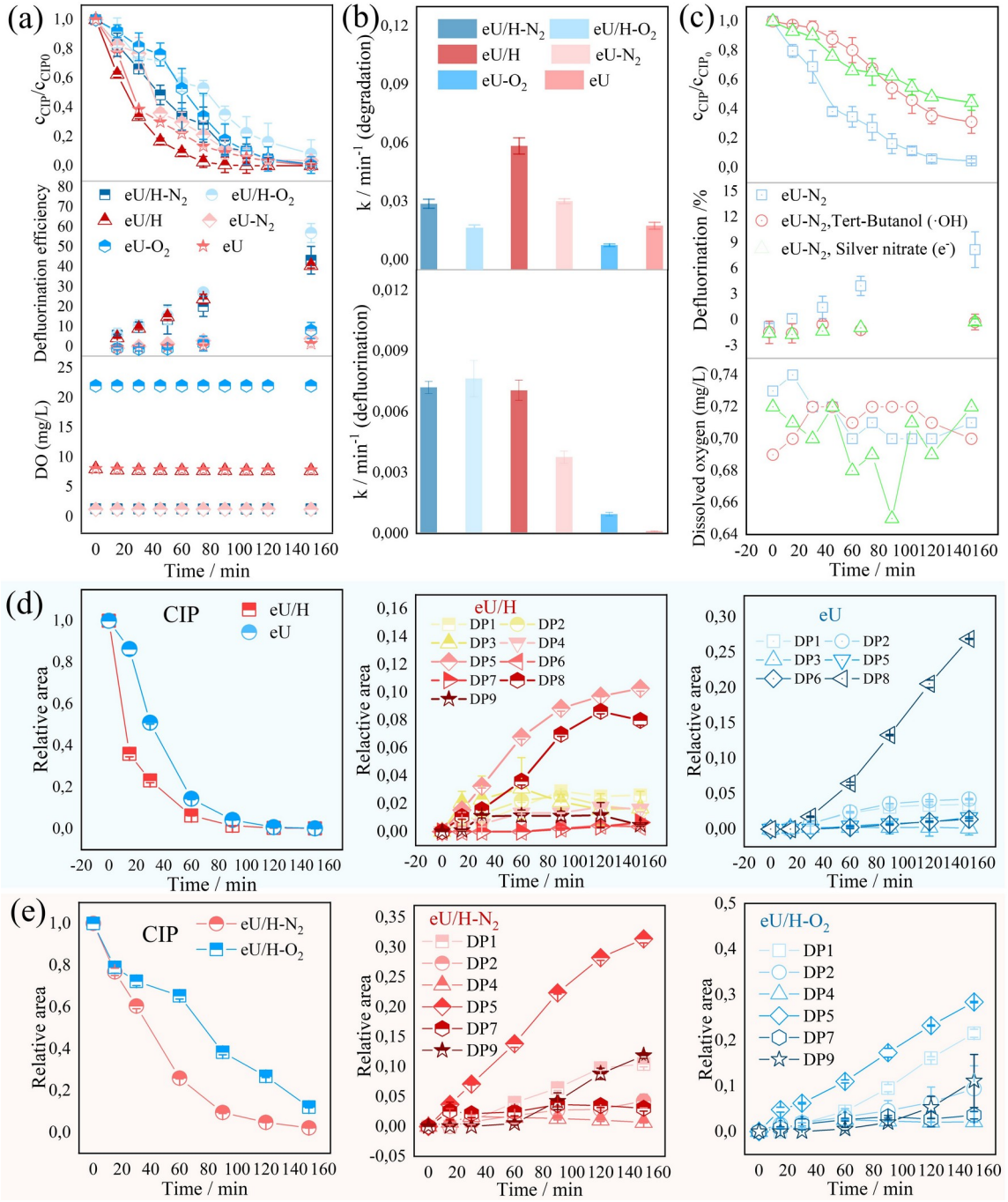


Fig. 6 Effect of dissolved oxygen on CIP degradation and defluorination by etched UCN and etched UCN/H_2O_2 (a-b); conditions: O_2/N_2 flow rate = 0.1 L/min, $[CIP]_0$ = 5 mg/L (with $[F]_0$ = 0.287 mg/L), initial pH ≈ 6.0, [etched UCN] = 0.5 g/L, [H_2O_2] = 20 mM, and simulated solar light; and scavenger tests on CIP degradation and defluorination by etched UCN with N_2 purging (c); conditions: N_2 flow rate = 0.1 L/min, [tert-butyl alcohol] = 10 mM and [silver nitrate] = 10 mM. Time-dependent evolution of CIP and its intermediates in different processes: etched UCN/H_2O_2 and etched UCN (d), etched UCN/H_2O_2 and etched UCN with gas purging (e). The processes of etched UCN and etched UCN/ H_2O_2 (20 mM) are denoted as eU and eU/H, respectively, in this figure.

3.5 Mechanism for the improved photocatalytic performance of etched UCN

The significantly improved performance of etched UCN on the photocatalytic degradation of CIP has been sufficiently demonstrated above. Based on the above results, the underlying mechanism could be

mainly attributed to the modified porous structure and tuned electronic and band structure of etched UCN compared to its pristine counterpart. The TEM and BET results confirmed that more pores were newly generated in the etched UCN, providing more active sites for CIP adsorption and subsequent photocatalytic degradation. The XRD and FTIR results indicate the incorporation of nitrogen vacancies in etched UCN by $NaBH_4$ treatment. The DRS and Mott–Schottky results show that the incorporated nitrogen vacancies tuned the band and electronic structures of the etched UCN. The light absorption range was extended from 462 to 484 nm, and the band gap of the etched UCN decreased from 2.69 eV to 2.12 eV, which is beneficial for improving the separation of photogenerated electron-hole pairs. The conduction band potential of etched UCN was estimated to be -0.42 eV (vs. NHE), which is negative enough for the formation of $\cdot O_2^-$. In contrast, the conduction band potential of pristine UCN (-0.18 eV vs. NHE) was not enough to induce the generation of $\cdot O_2^-$. Quenching tests confirmed that $^1O_2$ and $\cdot O_2^-$ play dominant roles in CIP degradation.

3.6 Degradation and defluorination mechanisms

First, UHPLC-QTOF/MS analysis was performed to investigate the formation of degradation products (DPs) and possible pathways involved in different processes under simulated solar light irradiation: etched UCN, etched UCN/H_2O_2, etched UCN/H_2O_2 with N_2 purging and etched UCN/H_2O_2 with O_2 purging. In total, nine different DPs, including four F-free intermediates (i.e., DP3, DP4, DP7 and DP9), were determined (Table S3 in the Supporting Information) during the process with etched UCN/H_2O_2. Fig. 6(d-e) displays the time-dependent evolution of these identified DPs. Few F-free intermediates were detected in the process with etched UCN, which is consistent with the limited defluorination observed during this process. In addition, the relative abundance of generated F-containing intermediates in the process with etched UCN increased with increasing illumination time, while that in the process with etched UCN/H_2O_2 first increased and then decreased with further irradiation, indicating lower degradation of CIP in the absence of H_2O_2. DP5 was the dominant intermediate in the process of etched UCN/H_2O_2 with N_2 purging and etched UCN/H_2O_2 with O_2 purging. In addition, as shown in Fig. S8 and Table S3 in the supporting information, no F-free intermediates were detected in the process of etched UCN with N_2 purging or in the presence of tert-butyl alcohol or silver nitrate (acting as ·OH and electron scavengers), further confirming the important indirect intermediate role of electrons in the generation of ·OH and defluorination. In contrast, four F-free intermediates (DP3, DP4, DP7 and DP9) were identified in the processes of etched UCN/H_2O_2, etched UCN/H_2O_2 with N_2 purging and O_2 purging. For these processes, the relative area abundance of F-free intermediates in the first 20 min was relatively low, demonstrating that low defluorination occurred at the initial stage. With the degradation of CIP, more F-containing intermediates formed, and the concentration of detected F^- in the reacted solution gradually increased. This may be explained by the above proposed hypothesis that direct defluorination from CIP is more difficult than that from F-containing intermediates.

DFT calculations were performed to gain a better understanding of the CIP degradation and defluorination mechanisms. Based on the optimal degradation and defluorination performance at pH 6, the main CIP dissociations (zwitterionic CIP^{+-} and CIP^+) under these conditions were selected as the target species for DFT calculations to further explore the CIP degradation and defluorination pathways. Generally, the degradation of CIP induced by electrophilic agents (h^+, ·OH, and $^1O_2$), nucleophilic agents ($\cdot O_2^-$) or radicals (·OH, $\cdot O_2^-$) is defined as electrophilic, nucleophilic or radical attack, respectively [1,57]. Notably, $\cdot O_2^-$ also exhibits nucleophilicity owing to an extra electron in its π* antibonding orbitals [58]. Hence, $\cdot O_2^-$ is treated as both a nucleophilic agent and a radical agent for CIP degradation in the following discussion. The Hirschfeld charge distribution is utilized to quantify the electron-accepting and electron-donating capabilities of the atoms in CIP^{+-} and CIP^+, as shown in Table S3 and Table S4. The atoms with the most positive and negative Hirschfeld charges in CIP are susceptible to nucleophilic and electrophilic attacks, respectively [59]. The results demonstrated that the oxygen atoms (38, 40 and 41(O)) in CIP^{+-} and CIP^+ exhibit the most negative charges but are

difficult to react because of steric hindrance [60]. Fig. 7, Table S5 and Table S7 reveal the potential reactive sites in CIP according to the condensed dual descriptor (CDD), Fukui index, and ESP, where a more negative (positive) CDD value implies a greater tendency for electrophilic (nucleophilic) attacks, a greater Fukui index $f^-/f^+/f^0$ value suggests a preference for electrophilic/nucleophilic/radical attack, and a greater negative (positive) ESP value indicates greater nucleophilicity (electrophilicity) [59,61]. Fig. 7 (b-e) indicates that the piperazine ring in zwitterionic CIP^{+-} is preferential for nucleophilic and radical attack, while the carboxylic group is more favorable for electrophilic and radical attack. In contrast, CIP^+ is less reactive to electrophilic, nucleophilic and radical attacks. Fig. 7 (h) and (p) confirm that degradation occurs more easily in zwitterionic CIP^{+-} than CIP^+ due to the more concentrated charge distribution in zwitterionic CIP^{+-}. The larger dipole moment of zwitterionic CIP^{+-} (21.644693 a.u.) than that of CIP^+ (13.909935 a.u.) further confirms that the charges in CIP^{+-} tend to localize at the ends of the molecule for easier degradation. In addition, the HOMO (LUMO) values in Fig. 7(f-g) and (n-o), which represent potential electrophilic (nucleophilic) attack, imply potential electrophilic and nucleophilic reactions in the benzene ring. Furthermore, DFT analysis was combined with the identified degradation products to propose the tentative CIP photocatalytic degradation and defluorination pathways by etched UCN.

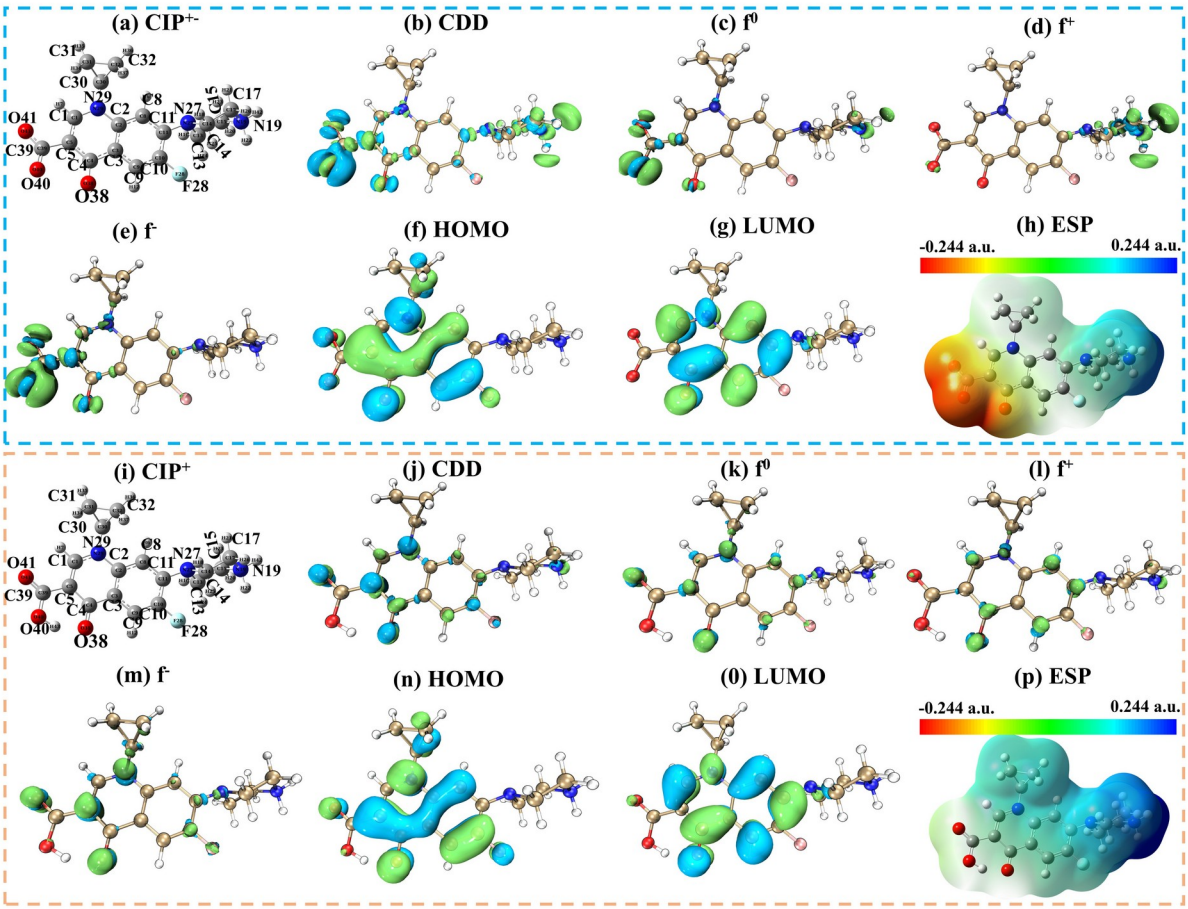


Fig. 7. Optimized molecular structure of CIP^{+-} (a), condensed dual descriptor (CDD) (b), Fukui index f^0 (c), f^+ (c), f^- (d), highest occupied molecular orbital (HOMO) (f) and lowest unoccupied molecular orbital (LUMO) (g) models, and electrostatic potential (ESP) diagram (h); optimized molecular structure of CIP^+ (i), condensed dual descriptor CDD (j), Fukui index f^0 (k), f^+ (l), f^- (m), HOMO (n) and LUMO (o) models, and ESP diagram (p).

As discussed above, the piperazine ring in CIP^+ is less reactive than that in CIP^{+-}. The 13(C), 14(C), 15(C) and 19(N) atoms of the piperazine ring in CIP^{+-} exhibit relatively greater CDD, f^+ and f^0 values than the other atoms, indicating that the piperazine ring is more susceptible to nucleophilic and radical

attacks by $\cdot O_2^-$ and ·OH. As proposed in pathway I in Fig. 8, $\cdot O_2^-$ attacks 15(C) in zwitterionic CIP^{+-} (CDD = 0.0305, f^+ = 00367) or CIP^+ (CDD = 0.0119, f^+ = 00177) to open the piperazine ring to form DP1, which can be further hydrolyzed to DP2 [62].

The 28(F) atom in zwitterionic CIP^{+-} and CIP^+ exhibits a relatively high negative Hirschfeld charge (i.e., -0.0982536529 a.u. and -0.0909521292 a.u.) and high negative CDD values (i.e., -0.0199 and -0.0184), implying that it is a favorable site for electrophilic attack by h^+, ·OH, and $^1O_2$. The Fukui index further revealed that the 28(F) atom in zwitterionic CIP^{+-} (f^- = 0.0200, f^0 = 0.0101) and CIP^+ (f^- = 0.0390, f^0 = 0.0298) is the preferential site for electrophilic and radical attack. Furthermore, the condensed local electrophilicity/nucleophilicity indices in Table S7 demonstrate that the 28(F) atom in zwitterionic CIP^{+-} has a distinctly greater nucleophilicity, confirming the possibility of electrophilic attack as well. Hence, CIP defluorination could occur by electrophilic and radical attacks. DP3, likely generated through the substitution of F by ·OH, was detected in the processes of etched UCN and etched UCN/H_2O_2, suggesting the possibility of direct defluorination from CIP [1]. As mentioned above, the C-F bond in CIP is a strong electron-withdrawing group, and ·OH is prone to react with a strong electron-donating group, suggesting that F substitution by ·OH is difficult. In a study by Wei *et al.*, DP3 was reported to be produced by hydroxide ion (OH^-) addition instead of ·OH substitution [52]. However, little defluorination was observed in the process with etched UCN under alkaline conditions in our experimental results, implying that F in CIP could hardly be substituted by OH^- directly. Considering the electron-withdrawing properties of C-F and ·OH and the distinctly inhibited defluorination in the electron scavenging test, it is therefore reasonable to speculate that the photogenerated electrons were also involved in assisting the defluorination process by ·OH substitution, as described in pathway II. In pathways III and IV, DP4, DP7 and DP9 were likely to be produced through C–F bond cleavage, indicating that not only electron-assisted ·OH substitution but also C–F bond cleavage could contribute to defluorination. This mechanism is consistent with previous reports of CIP defluorination by C–F bond cleavage [1,52,62]. Notably, DP4 is also likely derived from the direct cleavage of the C–F bond in CIP and the hydrolysis of DP3 (pathway V), whose relative area abundance is generally lower than that of the other F-containing intermediates (especially DP7 and DP9). Cleavage of the C-F bond of DP5 and opening of the piperazine ring in DP4 may both lead to the formation of DP7, while DP9 could be formed from the C-F bond cleavage of DP8 or further cleavage of the piperazine ring in DP7. It was also found that the relative area abundance of DP9 increased substantially after reacting for 75 min in the process of etched UCN/ H_2O_2 with N_2 purging compared to that in the process without N_2 purging, which may be attributed to the enhanced defluorination in this process.

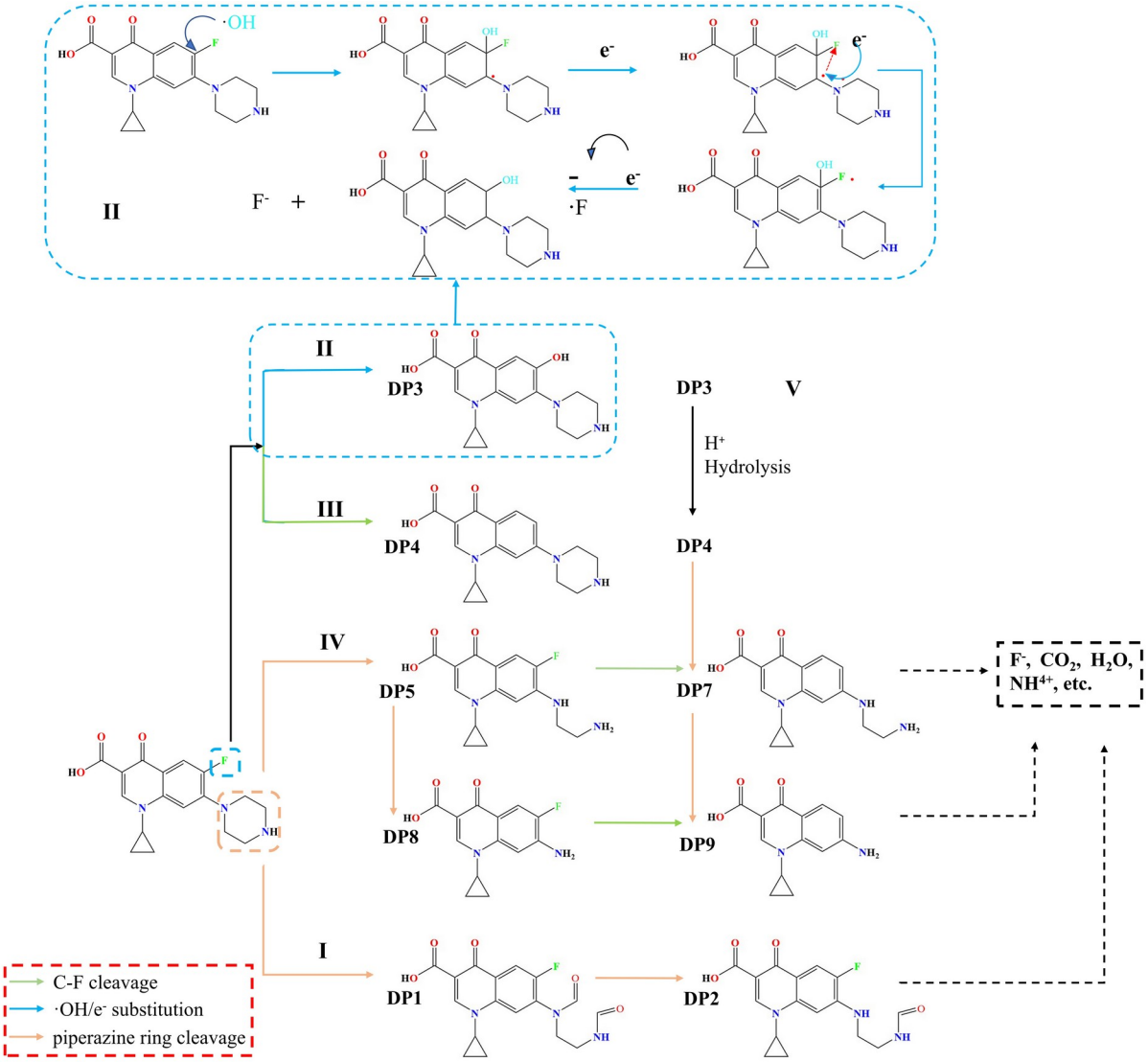
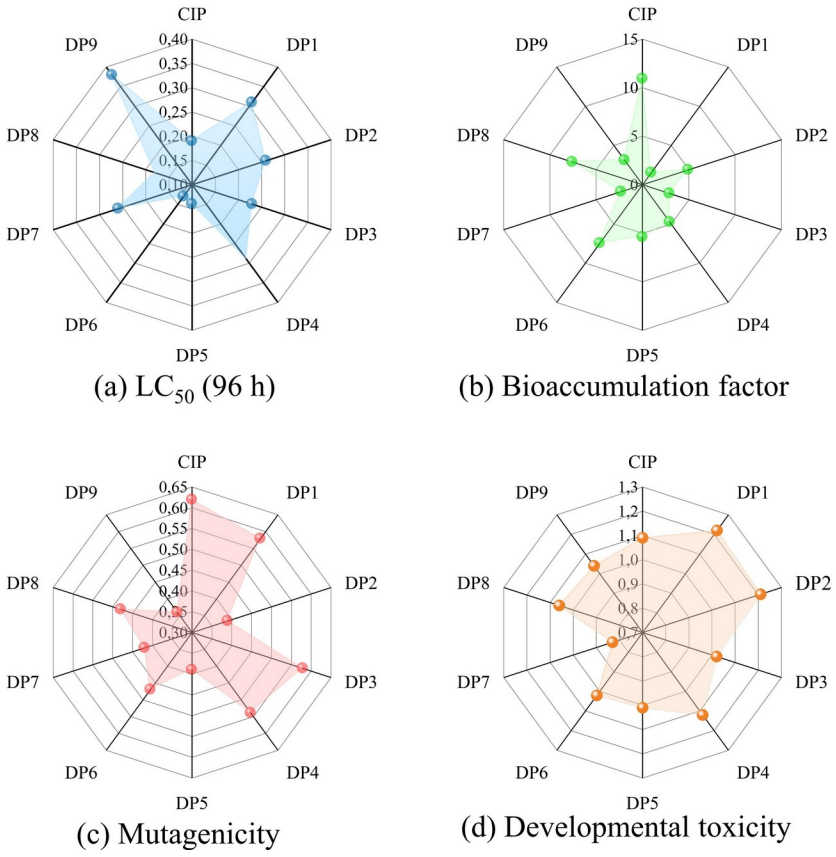


Fig. 8 Possible pathways for CIP degradation and defluorination

3.7 Toxicity evaluation

The toxicity of CIP and the generated intermediate products was evaluated using the toxicity estimation software TOOL based on quantitative structure-activity relationship (QSAR) analysis. As presented in Fig. 9, toxicity indicators, such as the bioaccumulation factor, mutagenicity, 96-hour fathead minnow LC_{50} and developmental toxicity, were assessed to monitor the changes in toxicity during the CIP photocatalytic degradation process. As demonstrated in Fig. 9(a), some F-containing intermediates, such as DP5 and DP6, exhibited lower LC_{50}-96 h values than did CIP, suggesting that incompletely degraded products (especially F-containing intermediates) may increase the toxicity to the ecosystem. In addition, the LC_{50}-96 h values of DP3, DP4, DP7 and DP9 increased compared to those of CIP, DP5 and DP9, implying that defluorination could reduce toxicity. From Fig. 9(b) and (c), the degree of potential harm caused by the bioaccumulation of degradation products (except for DP8) and mutagenicity generally decreased after CIP photocatalysis treatment. Specifically, non-F-containing intermediates, such as DP3, DP4, DP7 and DP9, had lower bioaccumulation factor and mutagenicity values than did CIP, DP6 and DP8, respectively, indicating that defluorination was beneficial for reducing the toxicity of CIP and its degradation products. Fig. 9(d) shows that most of

the intermediates, especially non-F-containing D3, D7 and D9, exhibited lower developmental toxicity than CIP.



(a) LC_{50} (96 h) (b) Bioaccumulation factor

(c) Mutagenicity (d) Developmental toxicity

Fig. 9 Assessment of the toxicity of CIP and its degradation intermediates

Conclusion

In this study, we confirmed the effects of the dominant reactive species on CIP degradation and defluorination in a visible light photocatalytic process with modified g-C_3N_4 and H_2O_2. $\cdot O_2^-$ and $^1O_2$ play dominant roles in CIP degradation. ·OH has a direct effect on the defluorination of CIP and F-containing intermediates, while electrons have an indirect effect on defluorination, acting as a critical intermediate to produce ·OH. The degradation and defluorination mechanisms were proposed based on the identification of degradation intermediates and the prediction of reactive sites via DFT calculations. Zwitterionic CIP^{+-} is much more reactive than CIP^+ due to the more concentrated charge distribution in zwitterionic CIP^{+-}, as indicated by the DFT results. The atoms in the piperazine ring of CIP have relatively higher CDD, f^+ and f^0 values than other atoms, providing active sites for nucleophilic and radical attacks by $\cdot O_2^-$ and ·OH. The experimental and theoretical investigation confirmed that the defluorination of CIP could be achieved mainly through electron-assisted ·OH substitution and C-F bond cleavage. The toxicity prediction results indicated that defluorination is beneficial for reducing the toxicity of antibiotic pollutants. However, the interaction effect on the generation of reactive species in the photocatalytic process, such as the intermediate role of electrons in ·OH generation in this study, deserves more attention.

Reference

[69] S. Li, T. Huang, P. Du, W. Liu, J. Hu, Photocatalytic transformation fate and toxicity of ciprofloxacin related to dissociation species: Experimental and theoretical evidences, Water Res 185 (2020) 116286. https://doi.org/10.1016/J.WATRES.2020.116286.

[70] X. Yu, J. Zhang, J. Zhang, J. Niu, J. Zhao, Y. Wei, B. Yao, Photocatalytic degradation of ciprofloxacin using Zn-doped Cu2O particles: Analysis of degradation pathways and intermediates, Chemical Engineering Journal 374 (2019) 316–327. https://doi.org/10.1016/J.CEJ.2019.05.177.

[71] A. Salma, S. Thoröe-Boveleth, T.C. Schmidt, J. Tuerk, Dependence of transformation product formation on pH during photolytic and photocatalytic degradation of ciprofloxacin, J Hazard Mater 313 (2016) 49–59. https://doi.org/10.1016/J.JHAZMAT.2016.03.010.

[72] H. Yuan, W. Shi, J. Lu, J. Wang, Y. Shi, F. Guo, Z. Kang, Dual-channels separated mechanism of photo-generated charges over semiconductor photocatalyst for hydrogen evolution: Interfacial charge transfer and transport dynamics insight, Chemical Engineering Journal 454 (2023) 140442. https://doi.org/10.1016/J.CEJ.2022.140442.

[73] X. Zhang, X. Zhang, P. Yang, S.P. Jiang, Layered graphitic carbon nitride: nano-heterostructures, photo/electro-chemical performance and trends, Journal of Nanostructure in Chemistry 2021 12:5 12 (2021) 669–691. https://doi.org/10.1007/S40097-021-00442-5.

[74] X. Zhang, P. Yang, Role of graphitic carbon in g-C3N4 nanoarchitectonics towards efficient photocatalytic reaction kinetics: A review, Carbon N Y 216 (2024) 118584. https://doi.org/10.1016/J.CARBON.2023.118584.

[75] A. Kumar, P. Raizada, A. Hosseini-Bandegharaei, V.K. Thakur, V.H. Nguyen, P. Singh, C-, N-Vacancy defect engineered polymeric carbon nitride towards photocatalysis: viewpoints and challenges, J Mater Chem A Mater 9 (2021) 111–153. https://doi.org/10.1039/D0TA08384D.

[76] V. Hasija, V.H. Nguyen, A. Kumar, P. Raizada, V. Krishnan, A.A.P. Khan, P. Singh, E. Lichtfouse, C. Wang, P. Thi Huong, Advanced activation of persulfate by polymeric g-C3N4 based photocatalysts for environmental remediation: A review, J Hazard Mater 413 (2021) 125324. https://doi.org/10.1016/J.JHAZMAT.2021.125324.

[77] E.M. Rodríguez, G. Márquez, M. Tena, P.M. Álvarez, F.J. Beltrán, Determination of main species involved in the first steps of TiO2 photocatalytic degradation of organics with the use of scavengers: The case of ofloxacin, Appl Catal B 178 (2015) 44–53. https://doi.org/10.1016/J.APCATB.2014.11.002.

[78] J. Sha, L. Li, Z. An, M. He, H. Yu, Y. Wang, B. Gao, S. Xu, Diametrically opposite effect of Cu2+ on sulfamerazine and ciprofloxacin adsorption-photodegradation in g-C3N4/visible light system: behavior and mechanism study, Chemical Engineering Journal 428 (2022) 131065. https://doi.org/10.1016/J.CEJ.2021.131065.

[79] V. Balakumar, M. Ramalingam, K. Sekar, C. Chuaicham, K. Sasaki, Fabrication and characterization of carbon quantum dots decorated hollow porous graphitic carbon nitride through polyaniline for photocatalysis, Chemical Engineering Journal 426 (2021) 131739. https://doi.org/10.1016/J.CEJ.2021.131739.

[80] X. Hu, X. Hu, Q. Peng, L. Zhou, X. Tan, L. Jiang, C. Tang, H. Wang, S. Liu, Y. Wang, Z. Ning, Mechanisms underlying the photocatalytic degradation pathway of ciprofloxacin with heterogeneous TiO2, Chemical Engineering Journal 380 (2020) 122366. https://doi.org/10.1016/J.CEJ.2019.122366.

[136] Y. Ohko, K.I. Iuchi, C. Niwa, T. Tatsuma, T. Nakashima, T. Iguchi, Y. Kubota, A. Fujishima, 17β-estradiol degradation by TiO2 photocatalysis as a means of reducing estrogenic activity, Environ Sci Technol 36 (2002) 4175–4181. https://doi.org/10.1021/ES011500A/ASSET/IMAGES/LARGE/ES011500AF00005.JPEG.

[140] X. Zhang, F. Wu, X.W. Wu, P. Chen, N. Deng, Photodegradation of acetaminophen in TiO2 suspended solution, J Hazard Mater 157 (2008) 300–307. https://doi.org/10.1016/J.JHAZMAT.2007.12.098.

[142] N.S. Alhokbany, R. Mousa, M. Naushad, S.M. Alshehri, T. Ahamad, Fabrication of Z-scheme photocatalysts g-C3N4/Ag3PO4/chitosan for the photocatalytic degradation of ciprofloxacin, Int J Biol Macromol 164 (2020) 3864–3872. https://doi.org/10.1016/J.IJBIOMAC.2020.08.133.

[146] H. Chi, J. Wan, Y. Ma, Y. Wang, M. Huang, X. Li, M. Pu, ZSM-5-(C@Fe) activated peroxymonosulfate for effectively degrading ciprofloxacin: In-depth analysis of degradation mode and degradation path, J Hazard Mater 398 (2020) 123024. https://doi.org/10.1016/J.JHAZMAT.2020.123024.

[148] Bioremediation of Industrial Waste for Environmental Safety, Bioremediation of Industrial Waste for Environmental Safety (2020). https://doi.org/10.1007/978-981-13-1891-7.

[150] H. Milh, X. Yu, D. Cabooter, R. Dewil, Degradation of ciprofloxacin using UV-based advanced removal processes: Comparison of persulfate-based advanced oxidation and sulfite-based advanced reduction processes, Science of The Total Environment 764 (2021) 144510. https://doi.org/10.1016/J.SCITOTENV.2020.144510.

[154] L. Yang, L. He, J. Xue, Y. Ma, Y. Shi, L. Wu, Z. Zhang, UV/SO32− based advanced reduction processes of aqueous contaminants: Current status and prospects, Chemical Engineering Journal 397 (2020) 125412. https://doi.org/10.1016/J.CEJ.2020.125412.

[157] M. Jiménez-Salcedo, M. Monge, M.T. Tena, Study of intermediate by-products and mechanism of the photocatalytic degradation of ciprofloxacin in water using graphitized carbon nitride nanosheets, Chemosphere 247 (2020) 125910. https://doi.org/10.1016/J.CHEMOSPHERE.2020.125910.

[160] L.W. Matzek, K.E. Carter, Sustained persulfate activation using solid iron: Kinetics and application to ciprofloxacin degradation, Chemical Engineering Journal 307 (2017) 650–660. https://doi.org/10.1016/J.CEJ.2016.08.126.

[163] Y. Li, L. Chen, X. Tian, L. Lin, R. Ding, W. Yan, F. Zhao, Functional role of mixed-culture microbe in photocatalysis coupled with biodegradation: Total organic carbon removal of ciprofloxacin, Science of The Total Environment 784 (2021) 147049. https://doi.org/10.1016/J.SCITOTENV.2021.147049.

[166] S. Luo, Z. Wei, D.D. Dionysiou, R. Spinney, W.P. Hu, L. Chai, Z. Yang, T. Ye, R. Xiao, Mechanistic insight into reactivity of sulfate radical with aromatic contaminants through single-electron transfer pathway, Chemical Engineering Journal 327 (2017) 1056–1065. https://doi.org/10.1016/J.CEJ.2017.06.179.

[174] Q. Mao, Y. Zhou, Y. Yang, J. Zhang, L. Liang, H. Wang, S. Luo, L. Luo, P. Jeyakumar, Y.S. Ok, M. Rizwan, Experimental and theoretical aspects of biochar-supported nanoscale zero-valent iron activating H2O2 for ciprofloxacin removal from aqueous solution, J Hazard Mater 380 (2019) 120848. https://doi.org/10.1016/J.JHAZMAT.2019.120848.

[175] B. Li, C. Lai, L. Qin, C. Chu, M. Zhang, S. Liu, X. Liu, H. Yi, J. He, L. Li, M. Li, L. Chen, Anchoring single-unit-cell defect-rich bismuth molybdate layers on ultrathin carbon nitride nanosheet with boosted

charge transfer for efficient photocatalytic ciprofloxacin degradation, J Colloid Interface Sci 560 (2020) 701–713. https://doi.org/10.1016/J.JCIS.2019.10.116.

[76] F. Guo, H. Zhang, H. Li, Z. Shen, Modulating the oxidative active species by regulating the valence of palladium cocatalyst in photocatalytic degradation of ciprofloxacin, Appl Catal B 306 (2022) 121092. https://doi.org/10.1016/J.APCATB.2022.121092.

[77] Z. Yang, L. Li, H. Yu, M. Liu, Y. Chi, J. Sha, S. Xu, Facile synthesis of highly crystalline g-C3N4 nanosheets with remarkable visible light photocatalytic activity for antibiotics removal, Chemosphere 271 (2021) 129503. https://doi.org/10.1016/J.CHEMOSPHERE.2020.129503.

[78] X. Song, W. Li, X. Liu, Y. Wu, D. He, Z. Ke, L. Cheng, C. Jiang, G. Wang, X. Xiao, Y. Li, Oxygen vacancies enable the visible light photoactivity of chromium-implanted TiO2 nanowires, Journal of Energy Chemistry 55 (2021) 154–161. https://doi.org/10.1016/J.JECHEM.2020.07.013.

[79] J. Zhu, H. Wang, A. Duan, Y. Wang, Mechanistic insight into the degradation of ciprofloxacin in water by hydroxyl radicals, J Hazard Mater 446 (2023) 130676. https://doi.org/10.1016/J.JHAZMAT.2022.130676.

[80] A. v. Marenich, C.J. Cramer, D.G. Truhlar, Universal solvation model based on solute electron density and on a continuum model of the solvent defined by the bulk dielectric constant and atomic surface tensions, Journal of Physical Chemistry B 113 (2009) 6378–6396. https://doi.org/10.1021/JP810292N/SUPPL_FILE/JP810292N_SI_003.PDF.

[81] Dennington R., Keith T.A., Millam J.M. Semichem Inc.;... - Google 学术搜索, (n.d.). https://scholar.google.com/scholar?hl=zh-CN&as_sdt=0%2C5&q=Dennington+R.%2C+Keith+T.A.%2C+Millam+J.M.+Semichem+Inc.%3B+Shawnee+Mission%2C+KS%3A+2016.+GaussView%2C+Version+6.1&btnG= (accessed March 4, 2023).

[82] H. Sun, F. Guo, J. Pan, W. Huang, K. Wang, W. Shi, One-pot thermal polymerization route to prepare N-deficient modified g-C3N4 for the degradation of tetracycline by the synergistic effect of photocatalysis and persulfate-based advanced oxidation process, Chemical Engineering Journal 406 (2021) 126844. https://doi.org/10.1016/J.CEJ.2020.126844.

[83] D. Zhao, C.-L. Dong, B. Wang, C. Chen, Y.-C. Huang, Z. Diao, S. Li, L. Guo, S. Shen, D. Zhao, B. Wang, Z. Diao, L. Guo, S. Shen, C. Dong, Y. Huang, C. Chen, S. Li, Synergy of Dopants and Defects in Graphitic Carbon Nitride with Exceptionally Modulated Band Structures for Efficient Photocatalytic Oxygen Evolution, Advanced Materials 31 (2019) 1903545. https://doi.org/10.1002/ADMA.201903545.

[84] X. Wu, X. Wang, F. Wang, H. Yu, Soluble g-C3N4 nanosheets: Facile synthesis and application in photocatalytic hydrogen evolution, Appl Catal B 247 (2019) 70–77. https://doi.org/10.1016/J.APCATB.2019.01.088.

[85] Z. Zhu, H. Pan, M. Murugananthan, J. Gong, Y. Zhang, Visible light-driven photocatalytically active g-C3N4 material for enhanced generation of H2O2, Appl Catal B 232 (2018) 19–25. https://doi.org/10.1016/J.APCATB.2018.03.035.

[86] Y. Wen, D. Qu, L. An, X. Gao, W. Jiang, D. Wu, D. Yang, Z. Sun, Defective g-C 3 N 4 Prepared by the NaBH 4 Reduction for High-Performance H 2 Production, ACS Sustain Chem Eng 7 (2019) 2343–2349. https://doi.org/10.1021/ACSSUSCHEMENG.8B05124/ASSET/IMAGES/LARGE/SC-2018-051244_0004.JPEG.

[37] M. Wu, Y. Gong, T. Nie, J. Zhang, R. Wang, H. Wang, B. He, Template-free synthesis of nanocage-like g-C3N4 with high surface area and nitrogen defects for enhanced photocatalytic H2 activity, J Mater Chem A Mater 7 (2019) 5324–5332. https://doi.org/10.1039/C8TA12076E.

[38] T. Yu, T. Xie, W. Zhou, Y. Zhang, Y. Chen, B. Shao, W.Q. Guo, X. Tan, Fumaric Acid Assistant Band Structure Tunable Nitrogen Defective g-C3N4Fabrication for Enhanced Photocatalytic Hydrogen Evolution, ACS Sustain Chem Eng 9 (2021) 7529–7540. https://doi.org/10.1021/ACSSUSCHEMENG.1C01163/ASSET/IMAGES/LARGE/SC1C01163_0009.JPEG.

[39] J. Zhang, X. Zhao, Y. Wang, Y. Gong, D. Cao, M. Qiao, Peroxymonosulfate-enhanced visible light photocatalytic degradation of bisphenol A by perylene imide-modified g-C3N4, Appl Catal B 237 (2018) 976–985. https://doi.org/10.1016/J.APCATB.2018.06.049.

[40] Z. Xie, Y. Feng, F. Wang, D. Chen, Q. Zhang, Y. Zeng, W. Lv, G. Liu, Construction of carbon dots modified MoO3/g-C3N4 Z-scheme photocatalyst with enhanced visible-light photocatalytic activity for the degradation of tetracycline, Appl Catal B 229 (2018) 96–104. https://doi.org/10.1016/J.APCATB.2018.02.011.

[41] T. Chen, Q. Zhang, Z. Xie, C. Tan, P. Chen, Y. Zeng, F. Wang, H. Liu, Y. Liu, G. Liu, W. Lv, Carbon nitride modified hexagonal boron nitride interface as highly efficient blue LED light-driven photocatalyst, Appl Catal B 238 (2018) 410–421. https://doi.org/10.1016/J.APCATB.2018.07.053.

[42] X. Zheng, Q. Zhang, T. Chen, Y. Wu, J. Hao, C. Tan, P. Chen, F. Wang, H. Liu, W. Lv, G. Liu, A novel synthetic carbon and oxygen doped stalactite-like g-C3N4 for broad-spectrum-driven indometacin degradation, J Hazard Mater 386 (2020) 121961. https://doi.org/10.1016/J.JHAZMAT.2019.121961.

[43] A. Mitra, P. Howli, D. Sen, B. Das, K.K. Chattopadhyay, Cu2O/g-C3N4 nanocomposites: an insight into the band structure tuning and catalytic efficiencies, Nanoscale 8 (2016) 19099–19109. https://doi.org/10.1039/C6NR06837E.

[44] G. Song, F. Qin, J. Yu, L. Tang, Y. Pang, C. Zhang, J. Wang, L. Deng, Tailoring biochar for persulfate-based environmental catalysis: Impact of biomass feedstocks, J Hazard Mater 424 (2022) 127663. https://doi.org/10.1016/J.JHAZMAT.2021.127663.

[45] X.F. Tan, S.S. Zhu, R.P. Wang, Y. di Chen, P.L. Show, F.F. Zhang, S.H. Ho, Role of biochar surface characteristics in the adsorption of aromatic compounds: Pore structure and functional groups, Chinese Chemical Letters 32 (2021) 2939–2946. https://doi.org/10.1016/J.CCLET.2021.04.059.

[46] Y. Wang, L. He, G. Dang, H. Li, X. Li, Preparation of Fe-MIL(100)-encapsulated magnetic g-C3N4 for adsorption of PPCPs from aqueous solution, Environmental Science and Pollution Research 28 (2021) 39769–39786. https://doi.org/10.1007/S11356-021-13550-0/FIGURES/8.

[47] H. Li, D. Zhang, X. Han, B. Xing, Adsorption of antibiotic ciprofloxacin on carbon nanotubes: pH dependence and thermodynamics, Chemosphere 95 (2014) 150–155. https://doi.org/10.1016/J.CHEMOSPHERE.2013.08.053.

[48] J. Choi, H. –H Kim, K. –M Lee, N. Chen, M.S. Kim, J. Seo, D. Lee, H. Cho, H. il Kim, J. Lee, H. Lee, C. Lee, Bicarbonate-enhanced generation of hydroxyl radical by visible light-induced photocatalysis of H2O2 over WO3: Alteration of electron transfer mechanism, Chemical Engineering Journal 432 (2022) 134401. https://doi.org/10.1016/J.CEJ.2021.134401.

[49] J. Lim, H. Kim, J. Park, G.H. Moon, J.J.M. Vequizo, A. Yamakata, J. Lee, W. Choi, How g-C3N4Works and Is Different from TiO2as an Environmental Photocatalyst: Mechanistic View, Environ Sci Technol

54 (2020) 497–506. https://doi.org/10.1021/ACS.EST.9B05044/ASSET/IMAGES/LARGE/ES9B05044_0006.JPEG.

[56] J. Tang, J. Wang, Fenton-like degradation of sulfamethoxazole using Fe-based magnetic nanoparticles embedded into mesoporous carbon hybrid as an efficient catalyst, Chemical Engineering Journal 351 (2018) 1085–1094. https://doi.org/10.1016/J.CEJ.2018.06.169.

[57] T. Li, L. Ge, X. Peng, W. Wang, W. Zhang, Enhanced degradation of sulfamethoxazole by a novel Fenton-like system with significantly reduced consumption of H2O2 activated by g-C3N4/MgO composite, Water Res 190 (2021) 116777. https://doi.org/10.1016/J.WATRES.2020.116777.

[58] X. Wei, J. Chen, Q. Xie, S. Zhang, L. Ge, X. Qiao, Distinct photolytic mechanisms and products for different dissociation species of ciprofloxacin, Environ Sci Technol 47 (2013) 4284–4290. https://doi.org/10.1021/ES400425B/SUPPL_FILE/ES400425B_SI_001.PDF.

[59] G. Liu, C. Feng, P. Shao, Degradation of Perfluorooctanoic Acid with Hydrated Electron by a Heterogeneous Catalytic System, Environ Sci Technol (2021). https://doi.org/10.1021/ACS.EST.1C06793/ASSET/IMAGES/LARGE/ES1C06793_0006.JPEG.

[60] G. V. Buxton, C.L. Greenstock, W.P. Helman, A.B. Ross, Critical Review of rate constants for reactions of hydrated electrons, hydrogen atoms and hydroxyl radicals (·OH/·O− in Aqueous Solution, J Phys Chem Ref Data 17 (2009) 513. https://doi.org/10.1063/1.555805.

[61] W. He, H.K. Kim, W.G. Wamer, D. Melka, J.H. Callahan, J.J. Yin, Photogenerated charge carriers and reactive oxygen species in ZnO/Au hybrid nanostructures with enhanced photocatalytic and antibacterial activity, J Am Chem Soc 136 (2014) 750–757. https://doi.org/10.1021/JA410800Y/SUPPL_FILE/JA410800Y_SI_001.PDF.

[62] G. Mamba, A.K. Mishra, Graphitic carbon nitride (g-C3N4) nanocomposites: A new and exciting generation of visible light driven photocatalysts for environmental pollution remediation, Appl Catal B 198 (2016) 347–377. https://doi.org/10.1016/J.APCATB.2016.05.052.

[63] C. Liu, S. Mao, M. Shi, F. Wang, M. Xia, Q. Chen, X. Ju, Peroxymonosulfate activation through 2D/2D Z-scheme CoAl-LDH/BiOBr photocatalyst under visible light for ciprofloxacin degradation, J Hazard Mater 420 (2021) 126613. https://doi.org/10.1016/J.JHAZMAT.2021.126613.

[64] L. Bai, Y. Jiang, D. Xia, Z. Wei, R. Spinney, D.D. Dionysiou, D. Minakata, R. Xiao, H. bin Xie, L. Chai, Mechanistic Understanding of Superoxide Radical-Mediated Degradation of Perfluorocarboxylic Acids, Environ Sci Technol 56 (2022) 624–633. https://doi.org/10.1021/ACS.EST.1C06356/ASSET/IMAGES/LARGE/ES1C06356_0005.JPEG.

[65] B. Wang, C. Rong, P.K. Chattaraj, S. Liu, A comparative study to predict regioselectivity, electrophilicity and nucleophilicity with Fukui function and Hirshfeld charge, Theor Chem Acc 138 (2019) 1–9. https://doi.org/10.1007/S00214-019-2515-1/TABLES/4.

[66] Q. Li, G. Wei, G. Duan, L. Zhang, Z. Li, Z. Wei, Q. Zhou, R. Pei, Photocatalysis activation of peroxydisulfate over oxygen vacancies-rich mixed metal oxide derived from red mud-based layered double hydroxide for ciprofloxacin degradation, Sep Purif Technol 289 (2022) 120733. https://doi.org/10.1016/J.SEPPUR.2022.120733.

[67] J. Cao, Q. Ren, F. Chen, T. Lu, Comparative study on the methods for predicting the reactive site of nucleophilic reaction, Sci China Chem 58 (2015) 1845–1852. https://doi.org/10.1007/S11426-015-5494-7/METRICS.

[828] J. Guo, H. Sun, X. Yuan, L. Jiang, Z. Wu, H. Yu, N. Tang, M. Yu, M. Yan, J. Liang, Photocatalytic degradation of persistent organic pollutants by Co-Cl bond reinforced CoAl-LDH/Bi12O17Cl2 photocatalyst: mechanism and application prospect evaluation, Water Res 219 (2022) 118558. https://doi.org/10.1016/J.WATRES.2022.118558.